

Control of discontinuous and continuous precipitation of γ' -strengthened high-entropy alloys through nanoscale Nb segregation and partitioning

L. Fan^a, T. Yang^b, J.H. Luan^b, Z.B. Jiao^{a,*}

^a *Department of Mechanical Engineering and Shenzhen Research Institute, The Hong Kong Polytechnic University, Hong Kong, China*

^b *Department of Materials Science and Engineering, City University of Hong Kong, Hong Kong, China*

Abstract: Control of discontinuous and continuous precipitation of L1₂-ordered γ' precipitates is crucial for tailoring microstructure and mechanical properties of coherent precipitation-strengthened high-entropy alloys (HEAs). In this study, we show that the appropriate addition of Nb not only suppresses discontinuous γ' precipitation through grain boundary segregation but also promotes continuous γ' precipitation through nanoscale solute partitioning, leading to substantially improved mechanical properties of the HEAs. Specifically, we explore the effects of Nb on the discontinuous and continuous precipitation microstructures, grain boundary segregation, and mechanical properties of (CoCrFeNi)_{94-x}Al₃Ti₃Nb_x ($x = 0, 0.4, 0.8, 1.6, \text{ and } 2.3 \text{ at.}\%$) HEAs. Atom probe tomography reveals that Nb exhibits preferential segregation at grain boundaries of HEAs, which substantially inhibits the grain boundary precipitation and migration due to the reduction of grain boundary energy and solute drag effect, thereby suppressing discontinuous γ' precipitation at the grain boundaries. Moreover, Nb partitions to the continuous γ' nanoparticles in grain interiors, which leads to a high chemical driving force for continuous γ' precipitation. Because of these beneficial effects, Nb-modified HEAs with a uniform distribution of γ' nanoparticles throughout

* Corresponding author. *E-mail address:* zb.jiao@polyu.edu.hk (Z.B. Jiao)

the matrix were developed, and the correlation between the precipitate microstructure and mechanical properties of these HEAs is discussed.

Keywords: High-entropy alloy; Nanoscale precipitation; Grain boundary segregation; Atom probe tomography; Precipitation strengthening

1. Introduction

High-entropy alloys (HEAs), also referred to as multi-principal element alloys, have emerged as an exciting new class of metallic materials [1-5]. Contrary to the general physical metallurgy intuition, these compositionally complex alloys containing multiple constituent elements—usually four or more—in equal or near equal concentrations tend to crystallize as single-phase solid solutions with simple crystal structures [6,7]. Among these alloys, the face-centered cubic (FCC) HEAs have received considerable attention because of their unique mechanical properties such as exceptional ductility and toughness, even down to the liquid nitrogen temperature [8-10]. However, these solid-solution alloys are relatively weak in strength, which is far from the requirements for practical structural applications [11-13]. Consequently, extensive efforts have been made to strengthen HEAs through various strengthening mechanisms [14-22]. In particular, the precipitation of coherent $L1_2$ -ordered γ' -Ni₃(Al,Ti) nanoparticles has been proved to be a powerful method for strengthening FCC HEAs without causing a significant loss of ductility because they can precipitate on a sufficiently fine scale by forming a microstructure analogous to γ/γ' Ni-based superalloys [23-30]. The degree of precipitation strengthening is highly dependent upon precipitate microstructural characteristics, including precipitate size, number density, and spatial distribution [31]. Thus, for an understanding of and eventually control over the microstructure and mechanical

properties of γ' -strengthened HEAs, it is crucial to understand their precipitation behavior and mechanism in such complex alloy systems.

Fundamentally, the precipitation of $L1_2$ -ordered γ' -Ni₃(Al,Ti) in FCC HEAs takes place through two distinct competitive modes, namely continuous and discontinuous precipitation. Continuous precipitation (CP) generally involves the formation of fine γ' nanoparticles within grain interiors, whereas discontinuous precipitation (DP) occurs at grain boundaries and proceeds inwards by the cellular growth of alternating layers of γ' precipitates and γ matrix (with greatly reduced supersaturation) behind a moving grain boundary [32]. The DP behavior is significant in γ' -strengthened HEAs; for example, Zhao et al. reported that the volume fraction of DP colonies can be as high as 50% upon aging in the CoCrNi-based alloys [26]. Similar behavior was observed in a CoCrFeNi-based alloy [24]. He et al. reported that γ' precipitates in both DP and CP regions have the same crystal structure (i.e., ordered $L1_2$), and DP colonies cannot be suppressed by adjusting Al and Ti concentrations or changing annealing treatments [24]. Because DP colonies are coarse in size and non-uniform in distribution, they have significant implications for the mechanical properties of HEAs [32]. CP nanoparticles are primarily responsible for precipitation hardening, whereas the coarse and wide-spaced DP colonies provide a limited hardening capability. Moreover, because DP colonies are generally limited to the vicinity of grain boundaries, they provide potential sites for localized deformation and thus reduce workability. For example, Chang et al. revealed that coarse DP colonies can crack grain boundaries of CoCrFeNi-based HEAs at high temperatures, thus dramatically reducing hot ductility [33]. Therefore, the minimization or even complete suppression of the DP reaction is crucial for achieving the improved mechanical properties of γ' -strengthened HEAs. Micro-alloying has been recognized as a key method for inhibiting the DP reaction either by altering precipitation thermodynamics or changing

precipitation kinetics in numerous conventional alloys with one or two principal constituents [32]. However, in HEAs comprising multi-principal elements, there is a lack of systematic research into the effects of micro-alloying on the DP behavior, and a fundamental understanding of mechanisms for suppressing the DP reaction has not yet evolved in γ' -strengthened HEAs.

In this study, we show that minor additions of Nb to γ' -strengthened HEAs cannot only suppress the DP reaction but also promote the CP formation through grain boundary segregation and nanoscale solute partitioning. Grain boundary characteristics and precipitate microstructures, including precipitate size, number density, morphology, and composition, of the γ' -strengthened $(\text{CoCrFeNi})_{94-x}\text{Al}_3\text{Ti}_3\text{Nb}_x$ (at.%) HEAs with different Nb contents were thoroughly examined by electron microscopies and atom probe tomography (APT). Particular effort was made to understand the fundamental mechanism for suppressing the DP reaction and to elucidate the correlation between the precipitate microstructure and mechanical properties of the γ' -strengthened HEAs.

2. Experimental

Alloys with nominal compositions of $(\text{CoCrFeNi})_{94-x}\text{Al}_3\text{Ti}_3\text{Nb}_x$ (at.%) were prepared by arc-melting a mixture of the constituent elements with purity higher than 99.9 wt.% under a Ti-gettered argon atmosphere, and the alloys were then drop-cast into a copper mold of $50 \times 15 \times 3$ mm³. Table 1 presents the chemical compositions of five HEAs with different Nb additions. For simplicity, these alloys are hereafter referred to as 0Nb, 0.4Nb, 0.8Nb, 1.6Nb and 2.3Nb alloys. Ingots were homogenized for 2 h at 1150 °C and then cold-rolled for multiple passes, yielding a total reduction of approximately 66%. The rolled plates were subjected to recrystallization for 3 min at 1150 °C and then aged at 800 °C for various periods of time.

Sections of the heat-treated samples were polished using standard mechanical polishing procedures and chemically etched with a dilute aqua regia solution. The resulting microstructures were examined by scanning electron microscopy (SEM), energy dispersive X-ray spectroscopy (EDS), and X-ray diffraction (XRD). Transmission electron microscopy (TEM) specimens were prepared by ion-milling of mechanically pre-thinned foils to the electron-transparent thickness using a precision ion polishing system. TEM and selected area electron diffraction (SAED) measurements were conducted on a JEM-2100F microscope operated at 200 kV. Needle-shaped specimens required for APT were fabricated by lift-outs and annular milled in an FEI Scios focused ion beam/scanning electron microscope (FIB/SEM). APT characterizations were performed in a CAMECA Instruments LEAP 5000XR local electrode atom probe. The specimens were analyzed in voltage mode, at a specimen temperature of 70 K, a pulse repetition rate of 200 kHz, a pulse fraction of 0.2, and an ion collection rate of 0.5% ions per field evaporation pulse. Imago Visualization and Analysis Software version 3.8 was used for three-dimensional reconstructions and data analysis.

Dog-bone shaped tensile specimens with a gauge length of 12.5 mm and a cross-section area of $3.2 \times 1 \text{ mm}^2$ were cut using electrical-discharge machining. Tensile tests were conducted at room temperature by using a MTS mechanical testing system at a strain rate of 10^{-3} s^{-1} . Fracture surfaces were examined by SEM. Thermodynamic calculations were employed to supplement and complement the experimental findings. Thermo-Calc 3.0 with Ni-database (TTNI8) was used to evaluate phase constitution and transformation.

3. Results

3.1. Microstructural characterization

Representative SEM micrographs of 0Nb, 0.4Nb, 0.8Nb, 1.6Nb, and 2.3Nb alloys aged for 8 h at 800 °C are presented in Fig. 1. The 0Nb alloy (Fig. 1a) exhibits a heterogeneous precipitate microstructure containing both CP and DP regions. The CP region consists of spherical γ' nanoparticles uniformly dispersed in the grain interior, whereas the DP region contains rod-shaped coarse γ' colonies near grain boundaries (Fig. 1b). The volume fraction of the DP region is approximately $30 \pm 6\%$, which is consistent with the previous reports in the CoCrFeNi-based HEAs [24,25]. With the 0.4% Nb addition, the CP and DP regions still coexist, but the volume fraction of the DP region is decreased to less than 10% (Fig. 1c). For the alloy with 0.8% Nb, the DP formation is almost completely suppressed, resulting in a uniform microstructure with continuous γ' nanoparticles throughout the matrix (Fig. 1d). However, with the further increase of Nb addition to 1.6 and 2.3 at.%, additional micron-sized block-shaped phases appear mostly at the grain boundaries (Figs. 1e and f). The EDS analysis reveals that these block-shaped phases are enriched with Nb and considerable amounts of Fe, Co, Cr and Ni (Fig. 2a), and the measured atomic ratio of (Fe + Co + Cr + Ni):(Nb + Ti) is approximately 2:1.

The phase structures of the 0Nb, 0.4Nb, 0.8Nb, 1.6Nb, and 2.3Nb alloys aged for 8 h at 800 °C were examined by XRD, and Fig. 2b shows the corresponding patterns. The 0Nb, 0.4Nb, and 0.8Nb alloys exhibit similar patterns, with γ and γ' peaks, validating that precipitates in the CP and DP regions have the same crystal structure. In the 1.6Nb alloy, although the peaks are prevalently indexed to the γ and γ' phases, a new diffraction peak at a 2θ of 41° corresponding to the Laves phase is also detected. Moreover, the Laves phase peak becomes prominent in the 2.3Nb alloy. The XRD patterns together with the EDS spectrum indicate the presence of Fe_2Nb -type block-shaped phases at grain boundaries. From these results, it can be concluded that 0.8 at.% Nb addition

is effective for suppressing the DP reaction without introducing the brittle Laves phase. Therefore, we investigate this alloy in detail in the following sections.

3.2. APT characterization of grain boundary segregation

Because the discontinuous γ' precipitates nucleate at grain boundaries, it is necessary to understand how Nb addition affects the grain boundary characteristics of the HEAs. The grain boundary chemistry of the 0.8Nb alloy in the as-recrystallized state was examined by APT, for which the required specimens were cut out and milled at a location containing grain boundaries using a site-specific FIB lift-out technique. The atom maps of Co, Cr, Fe, Ni, Al, Ti, and Nb from an APT dataset containing a grain boundary are shown in Fig. 3a. Clear segregation of Nb to the grain boundary is evident, and the planar feature of the segregation is clearly delineated in the iso-concentration surfaces of 2 at.% Nb. A quantitative compositional analysis of the grain boundary chemistry was conducted using one-dimensional concentration profiles. Figure 3b shows a representative profile of Nb, perpendicular across the grain boundary. The Nb content in grain interior regions is 0.8 ± 0.3 at.%, whereas the content at the grain boundary exhibits a maxima estimated to be 7.4 ± 0.8 at.%. To quantify the enrichments, the interfacial excess of Nb, which represents the number of excess Nb atoms at the grain boundary normalized to its area, is calculated to be approximately 3.5 atom/nm^2 .

3.3. Precipitate evolution in the DP region

Upon aging, coarse DP colonies are formed in the 0Nb alloy. To understand the DP mechanism, we investigate the temporal evolution of DP colonies by APT, and the required specimens were cut out from the DP region by using the site-specific FIB lift-out technique. As an

example, the APT microstructure of the DP region in the 2-h aged condition are shown in Fig. 4a, in which the relative positions and extents of Co (purple), Cr (pink), Fe (orange), Ni (green), Al (cyan), and Ti (blue) atoms are indicated. Because of the coarse size of discontinuous γ' precipitates, a part of a precipitate together with a part of the matrix can be observed in the volume of analysis. The partitioning of Ni, Ti, and Al to the precipitate and Co, Cr, and Fe to the matrix is clearly evident. Moreover, concentration isosurfaces with 12% (Al + Ti) were used to visualize the interface between the precipitate and matrix, and the corresponding proximity histogram based on concentration isosurfaces is displayed in Fig. 4b. Data points within the flat region of the profiles at the right side of the interface delineate the precipitate composition. The atomic ratio of Ni/Al in the precipitate is non-stoichiometric, and the average composition of the precipitate is 56.0Ni–7.0Al–18.9Ti–14.3Co–3.1Fe–0.8Cr at.%, thus yielding a (Ni + Co + Fe + Cr):(Al + Ti) ratio of approximately 3:1. Moreover, the precipitate microstructure in the DP region for 7.5-min and 8-h aged conditions were also examined by APT. The precipitate composition evolution as a function of aging time is summarized in Fig. 4c. The DP colonies exhibit no significant changes in composition with aging time, indicating the near-equilibrium nature of the DP colonies.

3.4 Precipitate evolution in the CP region

We now characterize the temporal evolution of continuous γ' nanoparticles in the CP region, the primary strengthening phases in the γ' -strengthened HEAs. The isosurfaces with a concentration of 12% (Al + Ti) were used to visualize CP nanoparticles. Figure 5 shows the CP microstructure of the 0Nb and 0.8Nb alloys in the 7.5-min, 2-h and 8-h aged conditions. High number densities of nanoparticles were detected in all the studied conditions, and the nanoparticles exhibit coarsening in both alloys with aging time while maintaining spherical morphology. The

proximity histograms of CP nanoparticles of 0Nb and 0.8Nb alloys are displayed in Fig. 6 as a function of aging time. In both alloys, the preferred partitioning of Co, Cr, and Fe to the matrix and Ni, Al, and Ti to the CP nanoparticles is evident. What is more interesting, and potentially relevant to an understanding of the formation mechanism of CP nanoparticles in FCC HEAs, is that Nb preferentially partitions towards CP nanoparticles; the concentration is approximately 2 at.% in the aged conditions. Moreover, the atomic ratio of (Ni + Co + Fe + Cr):(Ti + Al + Nb) in the 0.8Nb alloy is approximately 3:1, which is consistent with the formation of the (Ni,Co,Fe,Cr)₃(Ti,Al,Nb) phase.

TEM was employed to further examine the morphology and crystal structure of CP nanoparticles in the 0.8Nb alloy. A representative SAED pattern and a dark-field TEM (DF-TEM) image of the CP region in the 2-h aged condition are shown in Fig. 7. The SAED pattern clearly reveals the presence of (100) superlattice reflection in the [011] zone axis, which corresponds to a L1₂-ordered phase. The DF-TEM image of the CP region with the (100) superlattice spot exhibits the precipitation of high number densities of spherical nanoparticles with an average size of approximately 9 ± 3 nm, which is consistent with APT results. TEM observations together with the APT analysis demonstrate that the partitioning of Nb alters the composition but does not change the crystal structure of CP nanoparticles.

The average radius and number density of CP nanoparticles of the 0Nb and 0.8Nb alloys in the 7.5-min aged condition are shown in Fig. 8a. The average particle radii of the 0Nb and 0.8Nb alloys are 2.8 ± 0.8 and 3.0 ± 0.9 nm, respectively, whereas the number density of the 0.8Nb alloy ($7.9 \pm 0.9 \times 10^{23} \text{ nm}^{-3}$) is considerably larger than that of the 0Nb alloy ($6.1 \pm 1.0 \times 10^{23} \text{ nm}^{-3}$), indicating that Nb addition promotes the precipitation of CP nanoparticles. In the 2-h and 8-h aged conditions, CP nanoparticles are too coarse for quantitative analysis of sizes and number densities.

However, their compositions can be quantitatively determined, and based on these compositions, the volume fraction of the CP nanoparticles in different aging conditions can be estimated using the lever rule [34], as presented in Fig. 8b. The volume fraction of CP nanoparticles in the 0Nb alloy increases from 9.1 ± 0.9 at.% in the 7.5-min aged condition to 9.9 ± 0.7 at.% in the 2-h aged condition and to 10.2 ± 0.9 at.% in the 8-h aged condition, whereas that in the 0.8Nb alloy gradually increases from 11.5 ± 0.8 at.% in the 7.5-min aged condition to 12.0 ± 0.7 at.% in the 2-h aged condition and to 13.0 ± 0.5 at.% in the 8-h aged condition. Therefore, the Nb addition increases the volume fraction of CP nanoparticles in all the studied conditions, further confirming that Nb promotes γ' precipitation in the CP region of the γ' -strengthened HEAs.

3.5. Mechanical properties

Room-temperature tensile tests were performed to assess the effects of Nb additions on the mechanical properties of γ' -strengthened HEAs. The representative engineering stress–strain curves of the 0Nb, 0.4Nb, 0.8Nb, 1.6Nb, and 2.3Nb alloys aged for 8 h at 800 °C are shown in Fig. 9a, and the yield strength, ultimate tensile strength, elongation to failure, and reduction in area are summarized in Table 2. The 0Nb alloy exhibits a yield strength, ultimate tensile strength, elongation to failure, and reduction in area of approximately 636 ± 10 MPa, 1073 ± 9 MPa, $36 \pm 3\%$, and $72 \pm 10\%$, respectively. The addition of 0.4 at.% Nb slightly increases yield strength and ultimate tensile strength. By contrast, the 0.8 at.% Nb addition clearly increases yield strength and ultimate tensile strength ($\sim 770 \pm 13$ and $\sim 1129 \pm 17$ MPa, respectively), while maintaining a high ductility, with an elongation to failure of $\sim 32 \pm 2\%$ and a reduction in area of $79 \pm 6\%$. However, a further increase in Nb content significantly decreases ductility and reduces elongation to failure to approximately $22 \pm 6\%$ and $19 \pm 2\%$ for the 1.6Nb and 2.3Nb alloys, respectively, even though

a higher strength is achieved. Therefore, 0.8 at.% Nb addition is beneficial in increasing strength without decreasing ductility. To further evaluate the evolution of the hardening of the 0.8Nb alloy with respect to aging time, the as-recrystallized and aged samples with different aging times were evaluated (Fig. 9b and Table 2). Upon aging, the yield strength increases from 406 ± 13 MPa in the as-recrystallized condition to 729 ± 12 MPa in the 7.5-min aged condition and to 789 ± 9 MPa in the 2-h aged condition. With the further increase in the aging time, the strength gradually decreases to 770 ± 13 in the 8-h aged condition and further to 652 ± 10 MPa in the 32-h aged condition, indicating an overaging effect.

The fracture surfaces of the γ' -strengthened HEAs with different Nb additions after aging for 8 h at 800 °C are presented in Fig. 10. In the 0Nb alloy, the fracture surface reveals plenty of fine dimples, a characteristic mode of a ductile fracture (Fig. 10a). The addition of 0.4 and 0.8 at.% Nb does not induce apparent changes in the fracture mode, and the fracture surface still consists of numerous fine dimples (Figs. 10b and c). However, when the Nb content increases to 1.6 and 2.3 at.%, the fracture mode changes to a mixed fracture mode (Figs. 10d and e), with cleavage facets in areas surrounded by dimpled rupture or intergranular fracture features (Fig. 10f).

4. Discussion

The aforementioned results demonstrate that Nb additions are crucial for not only suppressing the DP reaction but also for promoting the CP formation of the γ' -strengthened HEAs. In the following sections, the mechanisms for suppressing DP colonies at grain boundaries and for promoting of CP nanoparticles in grain interiors are discussed in detail, and the correlation between the precipitate microstructure and mechanical properties of the γ' -strengthened HEAs is analyzed.

4.1 Mechanisms for the suppression of DP reaction at grain boundaries

Fundamentally, the DP reaction involves two critical steps, namely heterogeneous grain-boundary precipitation and synchronous grain-boundary migration, both of which are essentially determined by grain boundary properties. Our APT results reveal the prominent segregation of Nb at the grain boundaries of the HEAs, which may affect grain-boundary precipitation and/or migration. Therefore, the beneficial effects of Nb on the suppression of DP reaction are discussed in terms of (1) grain-boundary precipitation and (2) grain-boundary migration.

First, the effects of grain boundary Nb segregation on the grain boundary precipitation is analyzed. It is known that grain-boundary precipitation of a second phase is affected by such factors as grain-boundary energy and grain-boundary diffusion; the smaller these factors, the less likely the grain boundary precipitation occurs. The grain-boundary energy is affected significantly by the grain boundary segregation. In this study, the change in grain boundary energy caused by Nb segregation can be calculated by [35,36]:

$$\Delta\gamma = \Gamma(\Delta H_{seg} + kT\ln X) \quad (1)$$

where $\Delta\gamma$ is the grain-boundary energy variation, Γ is the specific Nb excess at the grain boundaries, ΔH_{seg} is the segregation enthalpy, kT represents the thermal energy (k is the Boltzmann constant and T is the temperature), and X is the Nb content in the alloy. ΔH_{seg} can be obtained using the McLean isotherm [37]:

$$\frac{X_{gb}}{1 - X_{gb}} = \frac{X_{gi}}{1 - X_{gi}} \exp\left(\frac{\Delta H_{seg}}{RT}\right) \quad (2)$$

where X_{gb} and X_{gi} are the Nb concentration at the grain boundary and grain interior, respectively, R is the gas constant, and T is the temperature. With input values of $\Gamma = 3.5 \text{ atom/nm}^2$, $k = 1.38 \times 10^{-23} \text{ J/K}$, $T = 1073 \text{ K}$, $X_{gb} = 7.4 \pm 0.8 \text{ at.}\%$, $X_{gi} = 0.8 \pm 0.3 \text{ at.}\%$, and $R = 8.31 \text{ J/K}\cdot\text{mol}$, the reduction in grain boundary energy caused by Nb segregation is $112.8 \pm 11.9 \text{ mJ/m}^2$ at $800 \text{ }^\circ\text{C}$. The relevant literature shows that the typical grain boundary energy of FCC CoCrFeNi-based alloys is approximately $630\text{--}900 \text{ mJ/m}^2$ at $800 \text{ }^\circ\text{C}$ [38-40]. Therefore, the reduction in grain boundary energy induced by Nb segregation is approximately 12–18% of the total grain boundary energy. Because the heterogeneous nucleation of DP γ' colonies is highly dependent on the extra energy provided by the grain boundaries, a dramatic reduction in grain boundary energy should increase the critical energy for nucleation, thereby thermodynamically inhibiting grain boundary precipitation. On the other hand, the grain boundary segregation of Nb can also affect the grain boundary precipitation by influencing the grain boundary diffusion. Since the diffusivity of Nb is considerably lower than that of the principal elements (i.e., Co, Cr, Fe, and Ni) because of its large atomic size and high melting point [5], the grain boundary precipitation would be retarded due to the lowering of grain boundary diffusivity. Consequently, the Nb segregation inhibits the grain boundary precipitation by reducing the grain-boundary energy and slowing down the grain-boundary diffusion, thereby substantially suppressing the DP initiation at the grain boundaries.

Second, the effects of grain boundary Nb segregation on the grain boundary migration is explored. From the thermodynamic point of view, grain boundary energy is one of the driving forces of grain boundary migration. As discussed above, the Nb segregation effectively reduces the grain boundary energy of the HEAs. Thus, the reduction in this energy by Nb segregation should inhibit the migration of grain boundaries. From the kinetic perspective, the grain boundary Nb segregation can interact with migrating grain boundaries through the solute-drag effect [41]. During grain boundary migration, the solute atmosphere formed by Nb segregation diffuses with but lags behind the grain boundary due to its considerably lower diffusivity [5], thus generating a dragging pressure on the grain boundary and kinetically reducing grain boundary mobility. In this study, Nb segregation is energetically favorable at the grain boundaries of CoCrFeNi-based HEAs, and the diffusivity of Nb is considerably lower than that of the principal elements (i.e., Co, Cr, Fe, and Ni) because of its large atomic size. Therefore, grain boundary migration can be substantially inhibited by the solute-drag of Nb, thus decelerating the kinetics of grain boundary migration in the Nb-modified HEAs. To further verify the effect of Nb segregation on grain boundary migration of HEAs, the recrystallization kinetics of three model alloys with different Nb additions—CoCrFeNi, (CoCrFeNi)_{99.5}Nb_{0.5} and (CoCrFeNi)₉₉Nb₁ (at.%)—were investigated. To eliminate the effect of γ' precipitates on the pinning of grain boundary migration, the Al and Ti additions were removed from the original HEAs, and thus the effect of Nb on the grain boundary migration behavior of HEAs can be evaluated. Cold-worked samples of these alloys were subjected to annealing at different temperatures, and the recrystallization temperature was determined by measuring micro-hardness and microstructure at different temperatures [42]. It is found that the Nb additions dramatically decelerate the kinetics of grain boundary migration, with the recrystallization temperature increasing from approximately 600 °C in the CoCrFeNi alloy to

approximately 725 °C in the (CoCrFeNi)_{99.5}Nb_{0.5} alloy and to approximately 775 °C in the (CoCrFeNi)₉₉Nb₁ alloy. Therefore, the Nb addition to the HEAs decreases the grain boundary mobility because of the reduction of grain boundary energy and solute-drag effect, which effectively inhibits the DP reaction at the grain boundaries.

The aforementioned analysis indicates that the grain boundary segregation of Nb is crucial in suppressing the (1) grain-boundary precipitation and (2) grain-boundary migration due to the combination of reduction of grain-boundary energy and solute-drag effects, both of which can substantially inhibit the DP reaction at the grain boundaries of the γ' -strengthened HEAs.

4.2 Mechanisms for the promotion of CP formation in grain interiors

In addition to suppressing the DP reaction, Nb addition also plays an important role in promoting CP formation, as evidenced by the higher number density and larger volume fraction of CP nanoparticles in the 0.8Nb alloy than those in the 0Nb alloy (Figs. 8a and b). Therefore, exploring the mechanism for the promotion of CP formation is crucial.

APT reveals that the 0.8Nb alloy has a higher number density of CP nanoparticles than the 0Nb alloy in the early stage of precipitation (the 7.5-min aged condition), which should not be a result of slow coarsening because the particle radius of the 0.8Nb alloy ($\sim 3.0 \pm 0.9$ nm) is larger than that of the 0Nb alloy ($\sim 2.8 \pm 0.8$ nm). Instead, the increased number density of CP nanoparticles is likely due to the enhanced nucleation by Nb. According to the classical nucleation theory, the critical energy for nucleation of a spherical precipitate (ΔG^*) is given by [43]:

$$\Delta G^* = \frac{16\pi\gamma^3}{3(\Delta G_v - \Delta G_e)} \quad (3)$$

where γ is the interfacial energy between the precipitate and matrix, ΔG_V is the chemical driving force for nucleation, and ΔG_ϵ is the elastic strain energy. The APT analysis indicates that no apparent interfacial segregation of Nb occurs at the interface between the precipitates and matrix, and thus it is unlikely that the Nb additions would change the interfacial energy of the precipitates. Moreover, the atomic size of Nb (143 pm) is very similar to that of Al (143 pm) and Ti (145 pm) [5], and thus, the partial substitution of Al and Ti by Nb in $(\text{Ni,Co})_3(\text{Al,Ti,Nb})$ precipitates is also unlikely to change the lattice mismatch between the precipitates and matrix [44]. Instead, the promotion of CP nanoparticles can be explained in terms of chemical driving force. The partitioning of Nb to the precipitates is equivalent to increasing the total concentration of the nanoparticle-forming elements. Therefore, the total supersaturation of Al, Ti, and Nb in the 0.8Nb alloy is higher than that of Al and Ti in the 0Nb alloy, which increases the chemical driving force for the nucleation of CP nanoparticles, thus increasing the number density of continuous γ' nanoparticles in the grain interior. As the CP and DP reactions are two competitive processes to lower the total free energy by consuming the solid-solution matrix, the promoted CP formation induced by the Nb partitioning would also slow down the DP reaction.

To further understand the promotion of CP reaction, we performed thermodynamic calculations using Thermo-Calc software to determine the effect of Nb concentration on the γ' phase. Figure 11a shows the calculated volume fraction of the γ' phase of the $(\text{CoCrFeNi})_{94-x}\text{Al}_3\text{Ti}_3\text{Nb}_x$ alloys as a function of temperature and Nb concentration. The volume fraction of the γ' phase increases from 15% in the 0Nb alloy to 20 % in the 0.8Nb alloy at 800 °C, which is in consistent with the experimental results. Moreover, the analysis of the theoretical phase compositions reveals that Nb is thermodynamically favorable to partition to the γ' phase, which increases the total concentration of γ' -forming elements and subsequently the volume fraction of

the γ' phase. However, a further increase of the Nb addition gradually decreases the γ' volume fraction because excessive Nb additions tend to induce the formation of the Laves phase (Fig. 11b). The Laves phase consumes the γ' -forming elements, including Ni and Nb, thereby reducing the volume fraction of the γ' phase. Therefore, thermodynamic calculations are consistent with our experimental observations that appropriate Nb addition (0.8 at.%) can promote γ' precipitation without forming the Laves phase.

On the basis of the aforementioned discussion on the DP and CP, the effects of Nb on the precipitation behavior of the γ' -strengthened HEAs can be summarized as follows and schematically illustrated in Fig. 12. In the Nb-free HEAs, the DP colonies are initiated at the grain boundaries, whereas the CP nanoparticles are formed in the grain interiors. As the precipitation reaction proceeds, both the CP nanoparticles and DP colonies grow, resulting in a microstructure containing a mixture of CP and DP regions. By contrast, in the HEAs with appropriate Nb additions, Nb tends to segregate at the grain boundaries, which inhibits both grain boundary precipitation and migration. Thus, the formation of DP colonies at grain boundaries is significantly suppressed. Moreover, Nb is energetically favorable to partition to the CP nanoparticles by forming $(\text{Ni,Co})_3(\text{Al,Ti,Nb})$ phase with increased number densities and volume fractions. Consequently, CP formation is the dominant precipitation routine in the Nb-modified HEAs, resulting in a microstructure containing a uniform distribution of CP nanoparticles throughout the matrix.

4.3 Precipitate-strengthening mechanisms for the γ' -nanoparticle-strengthened HEAs

Conventional γ' -strengthened HEAs generally comprise a large amount (more than 30 vol.%) of DP regions, in which DP colonies are irregular in both morphology and distribution, thus increasing the difficulty of modeling the strengthening response and of understanding the

strengthening mechanism. The results of this study indicate that an appropriate amount of Nb can completely suppress DP reaction, leading to the uniform distribution of CP nanoparticles throughout the matrix. Therefore, these Nb-modified alloys provide a suitable base on which to understand and model the precipitation strengthening contribution of γ' precipitates in the HEAs.

In precipitation-strengthened alloys, precipitates hinder dislocation motion by forcing them to shear weak obstacles (particle shearing) or bypass strong obstacles (Orowan bypass), depending on the precipitate size [45]. Because the critical precipitate size for the transition from particle shearing to Orowan bypass is unclear for the γ' -strengthened HEAs, the strengthening contribution of γ' nanoparticles is separately modeled using the two mechanisms. When the precipitates are strong obstacles, the increase in yield strength by the Orowan mechanism is given by [45]:

$$\Delta\sigma_{\text{orowan}} = \frac{0.4MGb \ln(2\bar{r}/b)}{\pi L_p \sqrt{1-\nu}} \quad (4)$$

where $M = 3$ is the Taylor factor, $G = 78.5$ GPa is the shear modulus for the matrix [24], $b = 0.255$ nm is the magnitude of the Burgers vector of the matrix [24], $\nu = 0.31$ is the Poisson ratio [24], $\bar{r} = \sqrt{2/3} \cdot r$ is the radius of the sphere particle on the slip planes, r is the average particle radius (Table 3), and $L_p = 2\bar{r}(\sqrt{\pi/(4f)} - 1)$ is the mean particle spacing. When the particles are weak, the particle shearing mechanism operates, and strengthening is primarily attributed to three parts, namely precipitate-matrix coherency ($\Delta\sigma_{\text{coherency}}$), modulus mismatch ($\Delta\sigma_{\text{modulus}}$), and atomic ordering ($\Delta\sigma_{\text{order}}$) [46-48]. The equations for the aforementioned particle shearing mechanism are as follows [45,49]:

$$\Delta\sigma_{\text{coherency}} = 2.6M(G\varepsilon)^{3/2} \left(\frac{rf}{0.5Gb} \right)^{1/2} \quad (5)$$

$$\Delta\sigma_{\text{modulus}} = 0.0055M(\Delta G)^{3/2}\left(\frac{2f}{G}\right)^{1/2}\left(\frac{r}{b}\right)^{3m/2-1} \quad (6)$$

$$\Delta\sigma_{\text{order}} = 0.81M\frac{\gamma_{APB}}{2b}\left(\frac{3\pi f}{8}\right)^{1/2} \quad (7)$$

where f is the volume fraction of the precipitates (Table 3), $\varepsilon \approx 2/3 \cdot (\Delta\alpha/\alpha)$ is the constrained lattice parameter mismatch, where $\Delta\alpha$ is the difference of lattice constant between the precipitates (3.590 Å) and the matrix (3.578 Å) [24,50], $\Delta G = 8.5$ GPa is the difference between the shear modulus of the γ' phase (87.0 GPa) and matrix (78.5 GPa) [24,51], $m = 0.85$ is a constant [45], and $\gamma_{APB} = 0.20$ J/m² is the anti-phase boundary energy of the γ' precipitates [52]. Using the experimental data obtained by APT and TEM (Table 3), the theoretical strengthening contributions from each individual mechanism were calculated and summarized in Table 3. The experimental values of precipitation strengthening were determined by the difference in yield strength between the aged and unaged samples of the 0.8Nb alloy and are also included in Table 3. The Orowan strengthening contribution is considerably higher than the experimental increment of yield strength in all conditions, implying that Orowan bypass mechanism might not be operative in the currently studied HEAs with ultrafine particles. For the particle shearing mechanism, the values of $\Delta\sigma_{\text{coherency}}$, $\Delta\sigma_{\text{modulus}}$, and $\Delta\sigma_{\text{order}}$ in the 7.5-min aged condition are approximately 29, 44, and 351 MPa, respectively; those for the 2-h aged condition are approximately 52, 61, and 361 MPa, respectively; those for the 8-h aged condition are approximately 70, 74, and 374 MPa, respectively. As suggested in Ref. [46], the increment in strengthening due to particle shearing is taken as the larger of (a) the sum of modulus strengthening and coherency strengthening ($\Delta\sigma_{\text{coherency}} + \Delta\sigma_{\text{modulus}}$), or (b) the order strengthening ($\Delta\sigma_{\text{order}}$). This is because these two modes (a and b) are sequential, the former occurring before the dislocation shears the particles and the latter during shearing. As

summarized in Table 3, $\Delta\sigma_{order}$ is much larger than $(\Delta\sigma_{coherency} + \Delta\sigma_{modulus})$ in all the aging conditions studied, suggesting that the precipitation strengthening should be contributed mainly by order strengthening. The contributions of order strengthening are approximately 351, 361, and 374 MPa for the 7.5-min, 2-h, and 8-h aged conditions, respectively, which are close to the experimental values of precipitation strengthening response, namely 323, 383, and 364 MPa, respectively (Table 3). Therefore, the particle shearing mechanism operates in the γ' -nanoparticle-strengthened HEAs, and order strengthening is crucial in the strengthening of these HEAs.

5. Conclusions

On the basis of the systematic investigation of the Nb effects on the discontinuous and continuous precipitate microstructures, grain boundary segregation, and mechanical properties of the $(\text{CoCrFeNi})_{94-x}\text{Al}_3\text{Ti}_3\text{Nb}_x$ HEAs, the following conclusions are drawn:

1. The precipitation of γ' precipitates in the CoCrFeNi-based HEAs occurs in the CP and DP modes. The Nb-free HEAs exhibit a microstructure containing CP nanoparticles in the grain interiors and DP colonies at grain boundaries. With an appropriate Nb addition (0.8 at.%), the coarse-sized DP colonies are completely suppressed, leading to the uniform distribution of CP nanoparticles throughout the matrix. However, excess additions of Nb can lead to the precipitation of Laves phase at grain boundaries.
2. APT reveals that Nb exhibits segregation at the grain boundaries of the CoCrFeNi-based HEAs. This segregation plays an important role in suppressing the (1) grain-boundary precipitation and (2) grain-boundary migration due to the synergistic effects of grain-boundary energy reduction and solute-drag effects, and the combination of these two factors significantly inhibits DP reaction in the γ' -strengthened HEAs.

3. In the CP region, APT reveals that Nb partitions to the γ' nanoparticles, the partitioning of which which increases the total concentration of the γ' -forming elements. This leads to a high chemical driving force for the γ' precipitation and also increases the volume fraction of γ' nanoparticles, which is in consistent with the thermodynamic calculations.
4. The 0.8Nb alloy, exhibiting a uniform distribution of γ' nanoparticles throughout the matrix, achieves a good combination of high strength and ductility. The modeling of precipitation strengthening indicates that the particle shearing mechanism is operative in the studied alloys with ultrafine particles, and order strengthening is crucial in the strengthening of the γ' -strengthened HEAs.

Acknowledgements

The authors would like thank Prof. C.T. Liu from City University of Hong Kong for fruitful discussion. This research was supported by the Early Career Scheme from the Research Grants Council of Hong Kong (25202719), National Science Foundation of China (51801169), and internal funding from The Hong Kong Polytechnic University (P0013862).

References

- [1] J.W. Yeh, S.K. Chen, S.J. Lin, J.Y. Gan, T.S. Chin, T.T. Shun, C.H. Tsau, S.Y. Chang, Nanostructured High-Entropy Alloys with Multiple Principal Elements: Novel Alloy Design Concepts and Outcomes, *Adv. Eng. Mater.* 6 (2004) 299-303.
- [2] B. Cantor, I.T.H. Chang, P. Knight, A.J.B. Vincent, Microstructural development in equiatomic multicomponent alloys, *Mater. Sci. Eng. A* 375-377 (2004) 213-218.
- [3] Y. Zhang, T.T. Zuo, Z. Tang, M.C. Gao, K.A. Dahmen, P.K. Liaw, Z.P. Lu, Microstructures and properties of high-entropy alloys, *Prog. Mater. Sci.* 61 (2014) 1-93.
- [4] E.P. George, D. Raabe, R.O. Ritchie, High-entropy alloys, *Nat. Rev. Mater.* 4 (2019) 1.
- [5] D.B. Miracle, O.N. Senkov, A critical review of high entropy alloys and related concepts, *Acta Mater.* 122 (2017) 448-511.
- [6] F. Otto, Y. Yang, H. Bei, E.P. George, Relative effects of enthalpy and entropy on the phase stability of equiatomic high-entropy alloys, *Acta Mater.* 61 (2013) 2628-2638.
- [7] C. Chattopadhyay, A. Prasad, B.S. Murty, Phase prediction in high entropy alloys—A kinetic approach, *Acta Mater.* 153 (2018) 214-225.
- [8] B. Gludovatz, A. Hohenwarter, D. Catoor, E.H. Chang, E.P. George, R.O. Ritchie, A fracture-resistant high-entropy alloy for cryogenic applications, *Science* 345 (2014) 1153-1158.
- [9] Z. Li, K.G. Pradeep, Y. Deng, D. Raabe, C.C. Tasan, Metastable high-entropy dual-phase alloys overcome the strength–ductility trade-off, *Nature* 534 (2016) 227-230.
- [10] Z. Li, S. Zhao, R.O. Ritchie, M.A. Meyers, Mechanical properties of high-entropy alloys with emphasis on face-centered cubic alloys, *Prog. Mater. Sci.* 102 (2019) 296-345.
- [11] F. Otto, A. Dlouhý, C. Somsen, H. Bei, G. Eggeler, E.P. George, The influences of temperature and microstructure on the tensile properties of a CoCrFeMnNi high-entropy alloy, *Acta Mater.* 61 (2013) 5743-5755.
- [12] H.Y. Diao, R. Feng, K.A. Dahmen, P.K. Liaw, Fundamental deformation behavior in high-entropy alloys: An overview, *Curr. Opin. Solid St. M.* 21 (2017) 252-266.
- [13] J. Miao, C.E. Slone, T.M. Smith, C. Niu, H. Bei, M. Ghazisaeidi, G.M. Pharr, M.J. Mills, The evolution of the deformation substructure in a Ni-Co-Cr equiatomic solid solution alloy, *Acta Mater.* 132 (2017) 35-48.

- [14] M. Choi, I. Ondicho, N. Park, N. Tsuji, Strength-ductility balance in an ultrafine-grained non-equiatomically $\text{Fe}_{50}(\text{CoCrMnNi})_{50}$ medium-entropy alloy with a fully recrystallized microstructure, *J. Alloy. Comp.* 780 (2019) 959-966.
- [15] P.J. Shi, W.L. Ren, T.X. Zheng, Z.M. Ren, X.L. Hou, J.C. Peng, P.F. Hu, Y.F. Gao, Y.B. Zhong, P.K. Liaw, Enhanced strength–ductility synergy in ultrafine-grained eutectic high-entropy alloys by inheriting microstructural lamellae, *Nat. Commun.* 10 (2019) 489.
- [16] L. Jiang, Z.Q. Cao, J.C. Jie, J.J. Zhang, Y.P. Lu, T.M. Wang, T.J. Li, Effect of Mo and Ni elements on microstructure evolution and mechanical properties of the $\text{CoFeNi}_x\text{VMo}_y$ high entropy alloys, *J. Alloy. Comp.* 649 (2015) 585-590.
- [17] D. Wei, X. Li, W. Heng, Y. Koizumi, F. He, W.M. Choi, B.J. Lee, H.S. Kim, H. Kato, A. Chiba, Novel Co-rich high entropy alloys with superior tensile properties, *Mater. Res. Lett.* 7 (2019) 82-88.
- [18] S.F. Liu, Y. Wu, H.T. Wang, W.T. Lin, Y.Y. Shang, J.B. Liu, K. An, X.J. Liu, H. Wang, Z.P. Lu, Transformation-reinforced high-entropy alloys with superior mechanical properties via tailoring stacking fault energy, *J. Alloy. Comp.* 792 (2019) 444-455.
- [19] C. Varvenne, A. Luque, W.A. Curtin, Theory of strengthening in fcc high entropy alloys, *Acta Mater.* 118 (2016) 164-176.
- [20] Z. Wu, C.M. Parish, Nano-twin mediated plasticity in carbon-containing FeNiCoCrMn high entropy alloys, *J. Alloy. Comp.* 647 (2015) 815-822.
- [21] Z. Li, C.C. Tasan, H. Springer, B. Gault, D. Raabe, Interstitial atoms enable joint twinning and transformation induced plasticity in strong and ductile high-entropy alloys, *Sci. Rep.* 7 (2017) 40704.
- [22] G. He, Y. Zhao, B. Gan, X. Sheng, Y. Liu, L. Tan, Mechanism of grain refinement in an equiatomically medium-entropy alloy CrCoNi during hot deformation, *J. Alloy. Comp.* 815 (2020) 152382.
- [23] T. Yang, Y.L. Zhao, Y. Tong, Z.B. Jiao, J. Wei, J.X. Cai, X.D. Han, D. Chen, A. Hu, J.J. Kai, K. Lu, Y. Liu, C.T. Liu, Multicomponent intermetallic nanoparticles and superb mechanical behaviors of complex alloys, *Science* 362 (2018) 933-937.

- [24] J.Y. He, H. Wang, H.L. Huang, X.D. Xu, M.W. Chen, Y. Wu, X.J. Liu, T.G. Nieh, K. An, Z.P. Lu, A precipitation-hardened high-entropy alloy with outstanding tensile properties, *Acta Mater.* 102 (2016) 187-196.
- [25] Y.Y. Zhao, H.W. Chen, Z.P. Lu, T.G. Nieh, Thermal stability and coarsening of coherent particles in a precipitation-hardened (NiCoFeCr)₉₄Ti₂Al₄ high-entropy alloy, *Acta Mater.* 147 (2018) 28-39.
- [26] Y.L. Zhao, T. Yang, Y. Tong, J. Wang, J.H. Luan, Z.B. Jiao, D. Chen, Y. Yang, A. Hu, C.T. Liu, J.J. Kai, Heterogeneous precipitation behavior and stacking-fault mediated deformation in a CoCrNi-based medium-entropy alloy, *Acta Mater.* 138 (2017) 72-82.
- [27] M.H. Chuang, M.H. Tsai, W.R. Wang, S.J. Lin, J.W. Yeh, Microstructure and wear behavior of Al_xCo_{1.5}CrFeNi_{1.5}Ti_y high-entropy alloys, *Acta Mater.* 59 (2011) 6308-6317.
- [28] Z. Fu, L. Jiang, J.L. Wardini, B.E. MacDonald, H. Wen, W. Xiong, D. Zhang, Y. Zhou, T.J. Rupert, W. Chen, E.J. Lavernia, A high-entropy alloy with hierarchical nanoprecipitates and ultrahigh strength, *Sci. Adv.* 4 (2018) eaat8712.
- [29] Y.J. Liang, L. Wang, Y. Wen, B. Cheng, Q. Wu, T. Cao, Q. Xiao, Y. Xue, G. Sha, Y. Wang, Y. Ren, High-content ductile coherent nanoprecipitates achieve ultrastrong high-entropy alloys, *Nat. Commun.* 9 (2018) 4063.
- [30] B. Gwalani, D. Choudhuri, V. Soni, Y. Ren, M. Styles, J.Y. Hwang, S.J. Nam, H. Ryu, S.H. Hong, R. Banerjee, Cu assisted stabilization and nucleation of L1₂ precipitates in Al_{0.3}CuFeCrNi₂ fcc-based high entropy alloy, *Acta Mater.* 129 (2017) 170-182.
- [31] R.C. Reed, *The Superalloys: Fundamentals and Applications*, first ed., Cambridge University Press, Cambridge, 2006.
- [32] D.B. Williams, E.P. Butler, Grain boundary discontinuous precipitation reactions, *Int. Met. Rev.* 26 (1981) 153-183.
- [33] Y.J. Chang, A.C. Yeh, The formation of cellular precipitate and its effect on the tensile properties of a precipitation strengthened high entropy alloy, *Mater. Chem. Phys.* 210 (2018) 111-119.
- [34] J.S. Van Sluytman, A. La Fontaine, J.M. Cairney, T.M. Pollock, Elemental partitioning of platinum group metal containing Ni-base superalloys using electron microprobe analysis and atom probe tomography, *Acta Mater.* 58 (2010) 1952-1962.

- [35] T. Chookajorn, H.A. Murdoch, C.A. Schuh, Design of stable nanocrystalline alloys, *Science* 337 (2012) 951-954.
- [36] R. Kirchheim, Grain coarsening inhibited by solute segregation, *Acta Mater.* 50 (2002) 413-419.
- [37] D. McLean, *Grain Boundaries in Metals*, first ed., Clarendon Press, Oxford, 1957.
- [38] S.V. Divinski, G. Replitz, G. Wilde, Grain boundary self-diffusion in polycrystalline nickel of different purity levels, *Acta Mater.* 58 (2010) 386-395.
- [39] D. Prokoshkina, V.A. Esin, G. Wilde, S.V. Divinski, Grain boundary width, energy and self-diffusion in nickel: effect of material purity, *Acta Mater.* 61 (2013) 5188-5197.
- [40] M. Vaidya, K.G. Pradeep, B.S. Murty, G. Wilde, S.V. Divinski, Radioactive isotopes reveal a non-sluggish kinetics of grain boundary diffusion in high entropy alloys, *Sci. Rep.* 7 (2017) 12293.
- [41] E. Hornbogen, Systematics of the cellular precipitation reactions, *Metall. Trans.* 3 (1972) 2717-2727.
- [42] Y. Lü, D.A. Molodov, G. Gottstein, Recrystallization kinetics and microstructure evolution during annealing of a cold-rolled Fe–Mn–C alloy, *Acta Mater.* 59 (2011) 3229-3243.
- [43] H.I. Aaronson, F.K. LeGoues, An assessment of studies on homogeneous diffusional nucleation kinetics in binary metallic alloys, *Metall. Trans. A* 23 (1992) 1915-1945.
- [44] G.D. Smith, S.J. Patel, The role of niobium in wrought precipitation-hardened nickel-base alloys, *Superalloys* 718 (2005) 625-706.
- [45] A.J. Ardell, Precipitation hardening, *Metall. Trans. A* 16 (1985) 1985-2131.
- [46] D.N. Seidman, E.A. Marquis, D.C. Dunand, Precipitation strengthening at ambient and elevated temperatures of heat-treatable Al(Sc) alloys, *Acta Mater.* 50 (2002) 4021-4035.
- [47] Y. Ma, Q. Wang, B.B. Jiang, C.L. Li, J.M. Hao, X.N. Li, C. Dong, T.G. Nieh, Controlled formation of coherent cuboidal nanoprecipitates in body-centered cubic high-entropy alloys based on $\text{Al}_2(\text{Ni}, \text{Co}, \text{Fe}, \text{Cr})_{14}$ compositions, *Acta Mater.* 147 (2018) 213-225.
- [48] K. Ming, X. Bi, J. Wang, Realizing strength-ductility combination of coarse-grained $\text{Al}_{0.2}\text{Co}_{1.5}\text{CrFeNi}_{1.5}\text{Ti}_{0.3}$ alloy via nano-sized, coherent precipitates, *Int. J. Plast.* 100 (2018) 177-191.

- [49] A. Kelly, R.B. Nicholson, *Strengthening Methods in Crystals*, first ed., Elsevier, New York, 1971.
- [50] R. Lawitzki, S. Hassan, L. Karge, J. Wagner, D. Wang, J. von Kobylinski, C. Kremaszky, M. Hofmann, R. Gilles, G. Schmitz, Differentiation of γ' - and γ'' - precipitates in Inconel 718 by a complementary study with small-angle neutron scattering and analytical microscopy, *Acta Mater.* 163 (2019) 28-39.
- [51] C.L. Fu, Y.Y. Ye, M.H. Yoo, *High-Temperature Order Intermetallic Alloys V*, *Mater. Res. Soc. Symp. Proc.* 288 (1993) 21-32.
- [52] M. Vittori, A. Mignone, On the antiphase boundary energy of $\text{Ni}_3(\text{Al,Ti})$ particles, *Mater. Sci. Eng.* 74 (1985) 29-37.

Figure captions

Fig. 1. Microstructures of the $(\text{CoCrFeNi})_{94-x}\text{Al}_3\text{Ti}_3\text{Nb}_x$ alloys in the 8-h aged condition: (a and b) 0Nb, (c) 0.4Nb, (d) 0.8Nb, (e) 1.6Nb, and (f) 2.3Nb. (b) is an enlarged view of the DP and CP regions in the 0Nb alloy.

Fig. 2. (a) EDS spectrum of the block-shaped phase in the 2.3Nb alloy, and (b) XRD patterns of the $(\text{CoCrFeNi})_{94-x}\text{Al}_3\text{Ti}_3\text{Nb}_x$ alloys in the 8-h aged condition.

Fig. 3. (a) SEM microstructure and atom maps of dataset containing grain boundaries of the as-recrystallized 0.8Nb alloy, and (b) 1D concentration profile of Nb across the grain boundary.

Fig. 4. (a) Atom maps of Co, Cr, Fe, Ni, Al, and Ti of the DP region of the 0Nb alloy in the 2-h aged condition, (b) proximity histograms of the DP region in the 2-h aged condition, and (c) evolution of precipitate composition of the DP region as a function of aging time.

Fig. 5. CP nanoparticles of the 0Nb and 0.8Nb alloys in different aging conditions: (a) 0Nb, 7.5 min, (b) 0Nb, 2 h, (c) 0Nb, 8 h, (d) 0.8Nb, 7.5 min, (e) 0.8Nb, 2 h, and (f) 0.8Nb, 8 h.

Fig. 6. Proximity histograms of CP nanoparticles of the 0Nb and 0.8Nb alloys in different aging conditions: (a) 0Nb, 7.5 min, (b) 0.8Nb, 7.5 min, (c) 0Nb, 2 h, (d) 0.8Nb 2 h, (e) 0Nb, 8 h, and (f) 0.8Nb, 8 h.

Fig. 7. (a) SAED pattern and (b) dark-field TEM image of the 0.8Nb alloy in the 2-h aged condition.

Fig. 8. (a) Particle radii and number densities of CP nanoparticles in the 0Nb and 0.8Nb alloys in the 7.5-min aged condition, and (b) volume fractions of CP nanoparticles in the 0Nb and 0.8Nb alloys as a function of aging time.

Fig. 9. Room-temperature tensile stress–strain curves of (a) the $(\text{CoCrFeNi})_{94-x}\text{Al}_3\text{Ti}_3\text{Nb}_x$ alloys in the 8-h aged condition and (b) 0.8Nb alloy in different aging conditions.

Fig. 10. Fracture surfaces of the $(\text{CoCrFeNi})_{94-x}\text{Al}_3\text{Ti}_3\text{Nb}_x$ alloys in the 8-h aged condition: (a) 0Nb, (b) 0.4Nb, (c) 0.8Nb, (d) 1.6Nb, and (e and f) 2.3Nb. (f) is an enlarged view of the fracture surface in (e).

Fig. 11. (a) Calculated volume fractions of γ' phase in the $(\text{CoCrFeNi})_{94-x}\text{Al}_3\text{Ti}_3\text{Nb}_x$ alloys, and (b) the pseudo-binary phase diagram of the $(\text{CoCrFeNi})_{94-x}\text{Al}_3\text{Ti}_3\text{Nb}_x$ system.

Fig. 12. Schematics showing the precipitation mechanism of the γ' -precipitate-strengthened HEAs with and without Nb additions.

Fig. 1

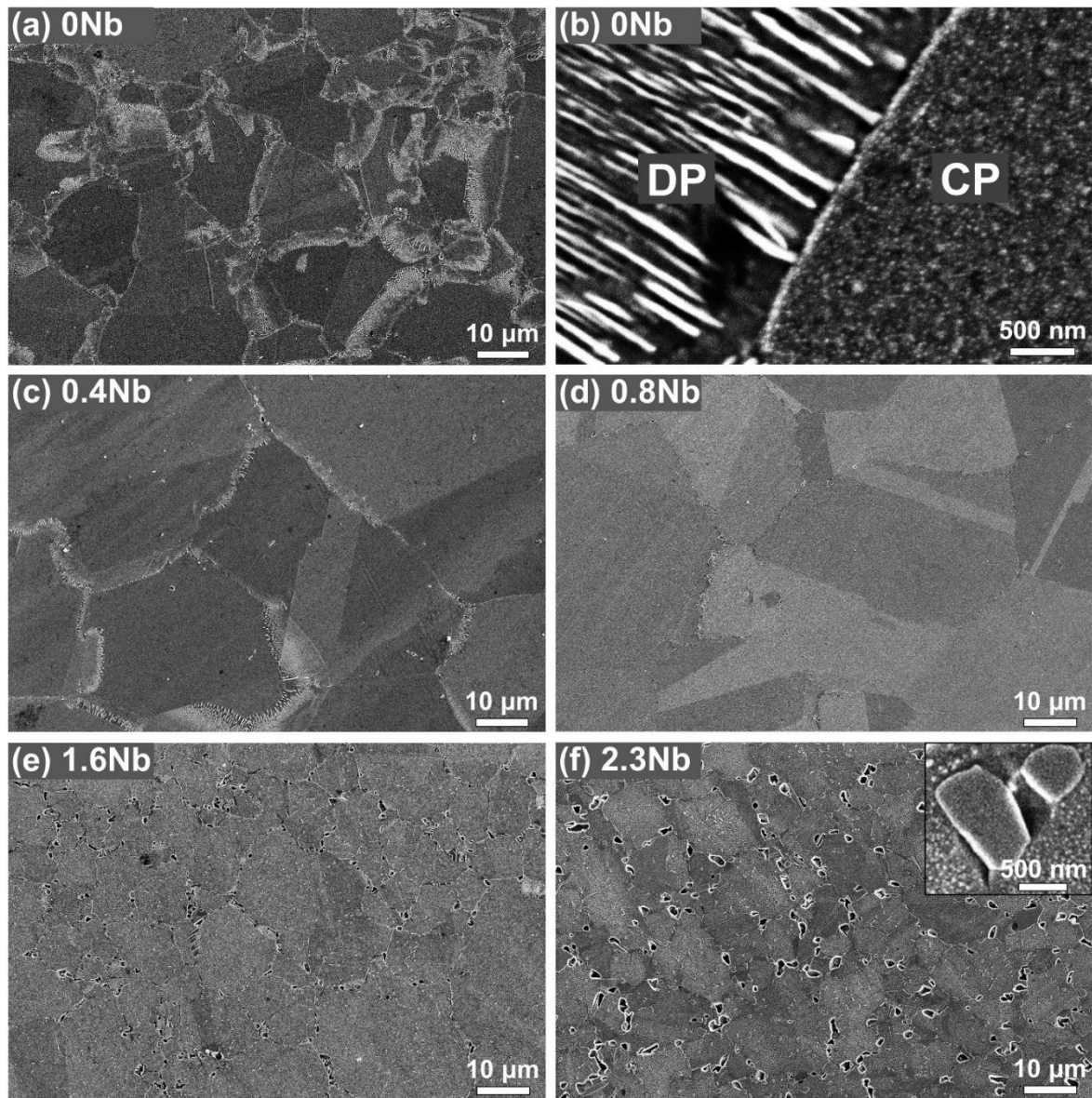


Fig. 2

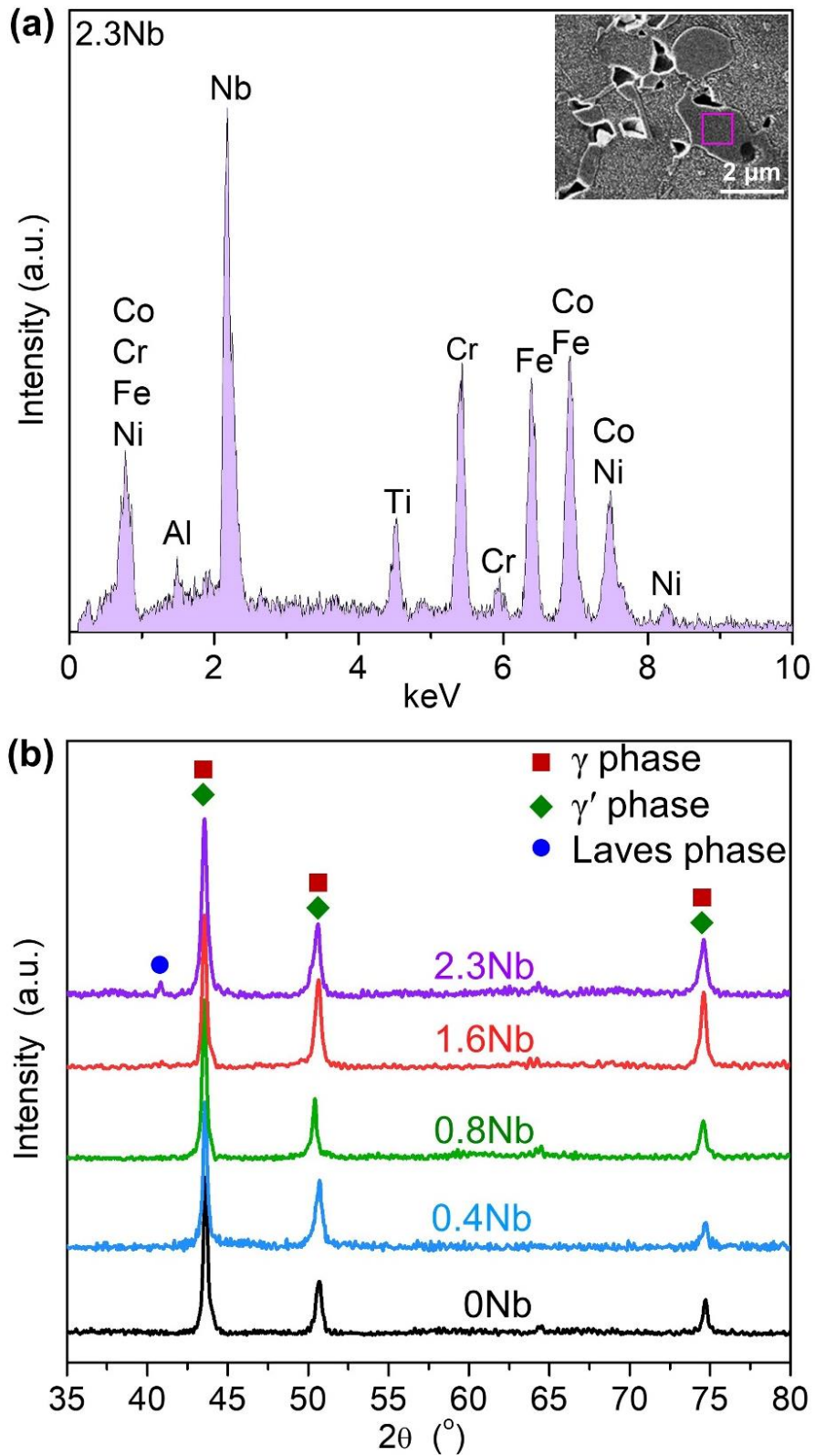


Fig. 3

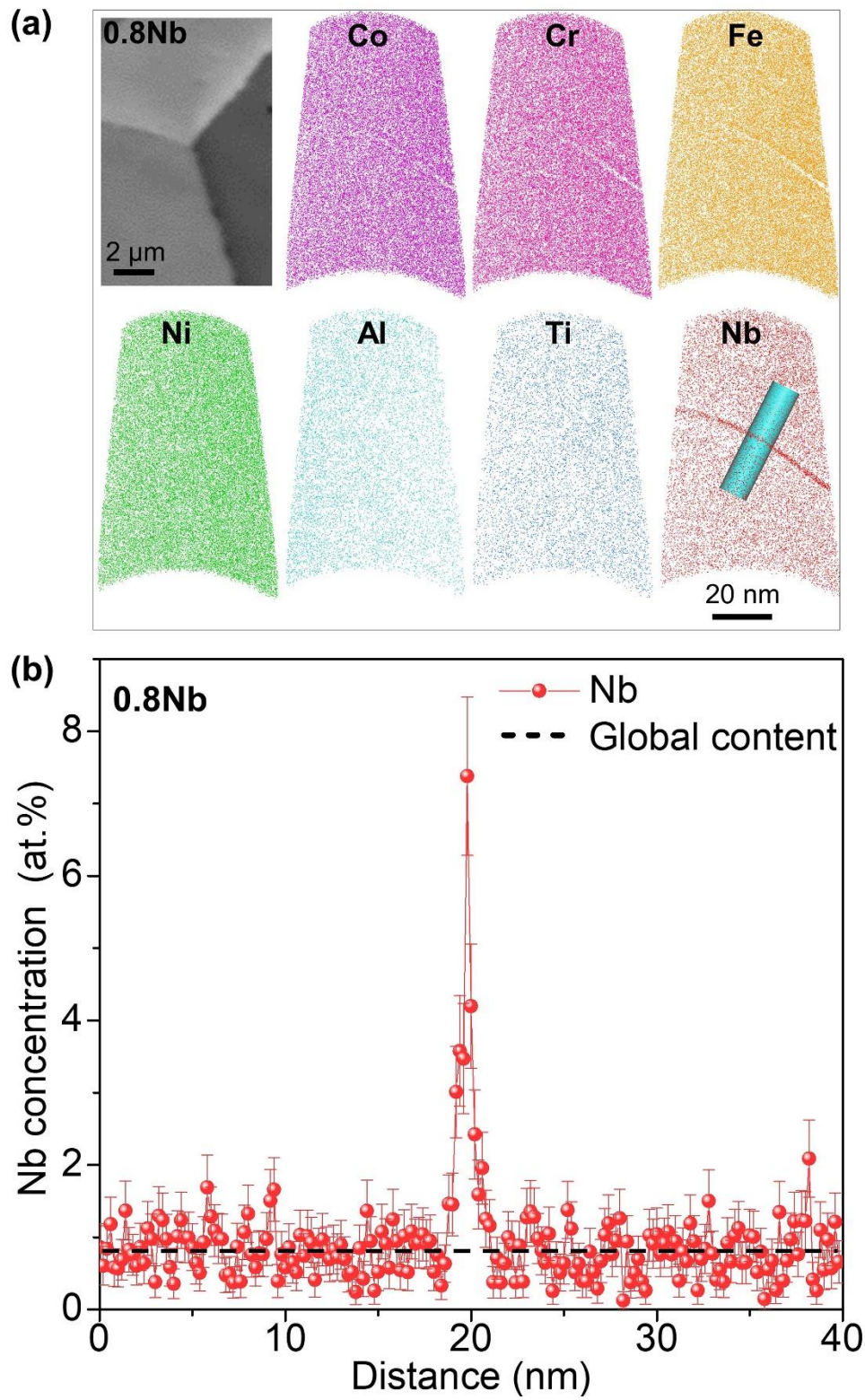


Fig. 4

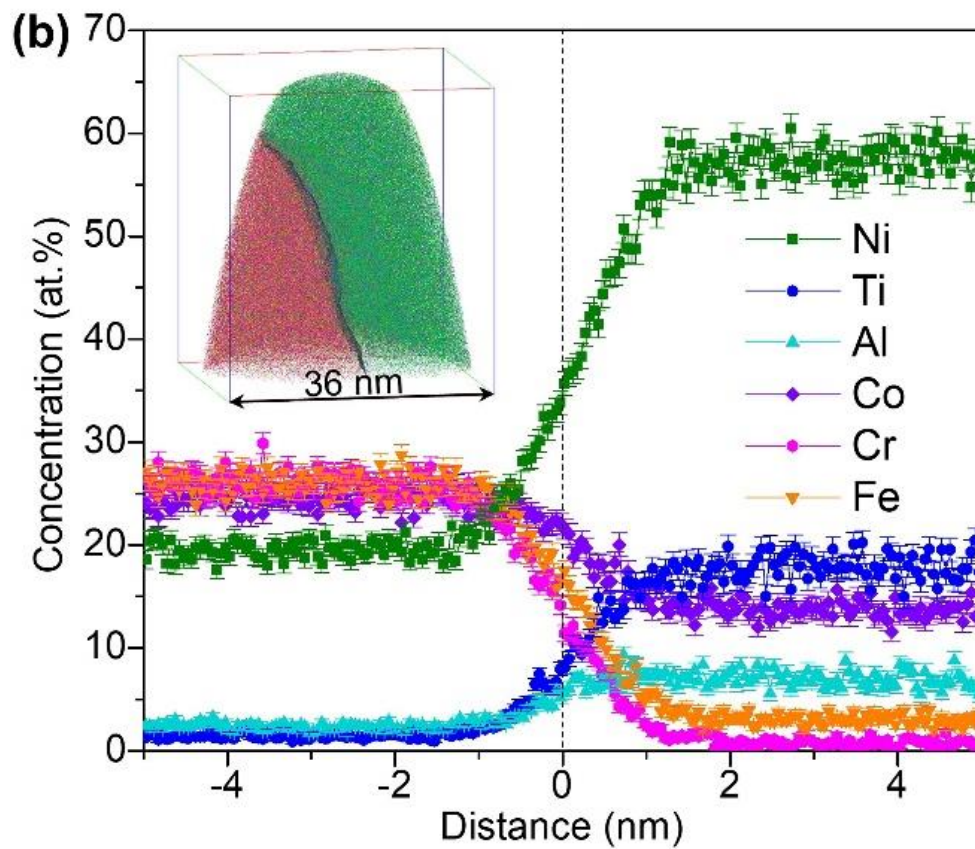
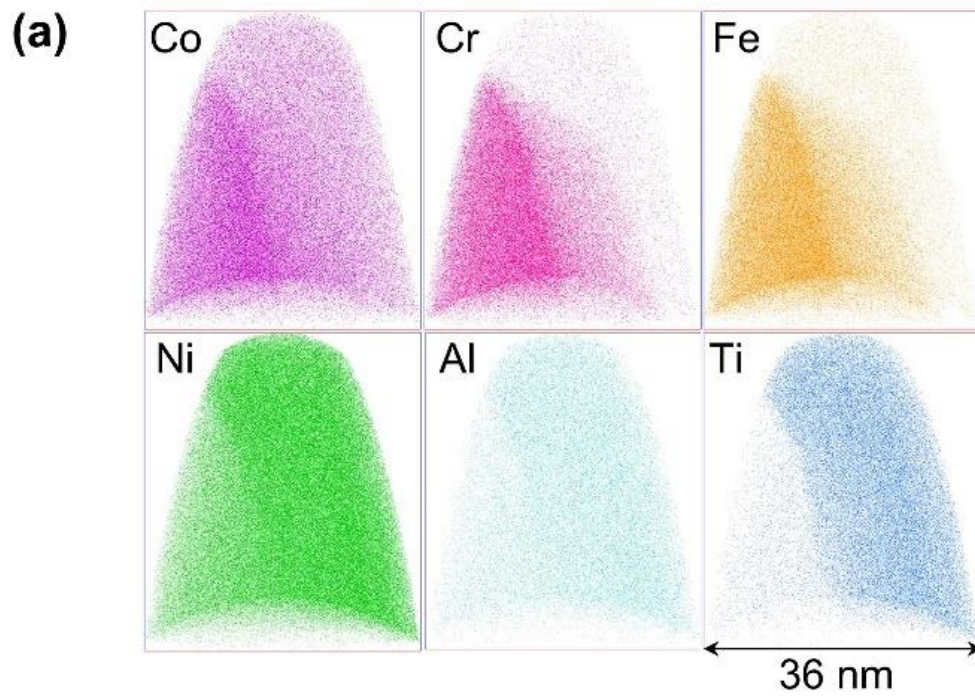


Fig. 4 (cont'd)

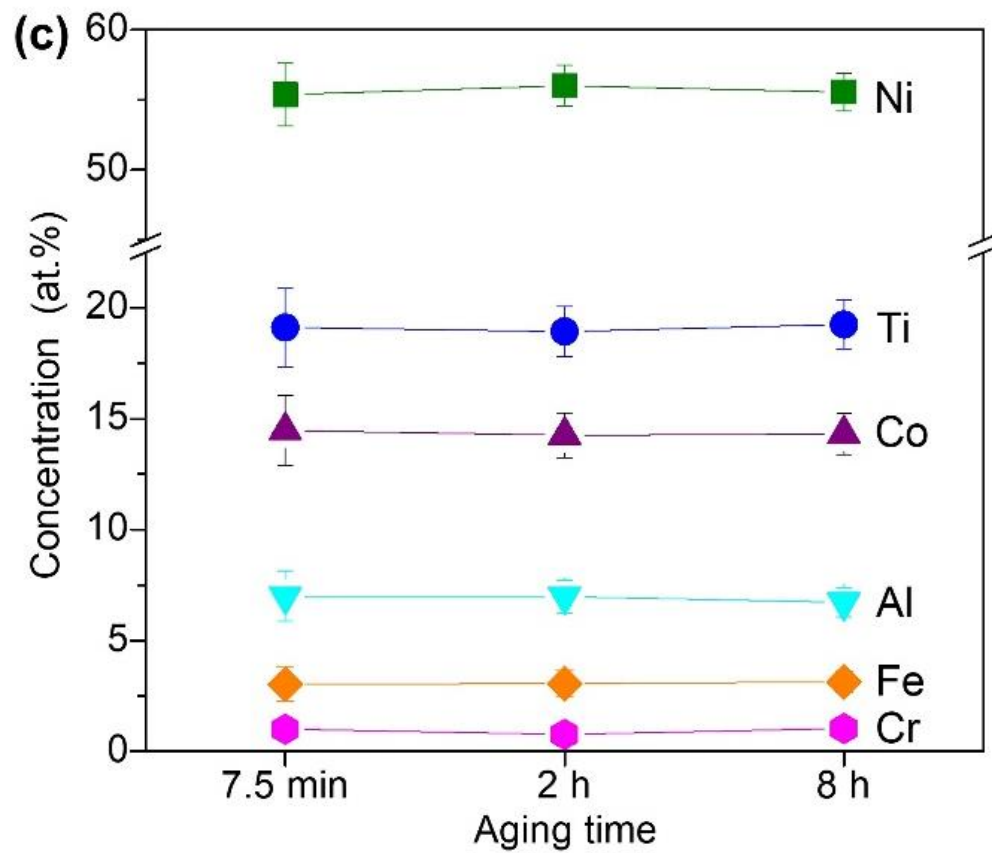
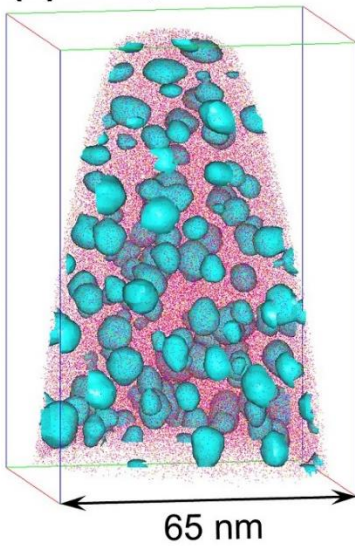
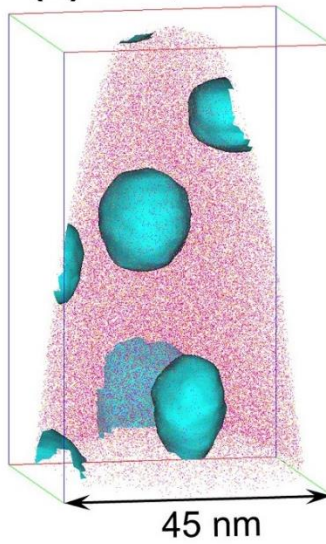


Fig. 5

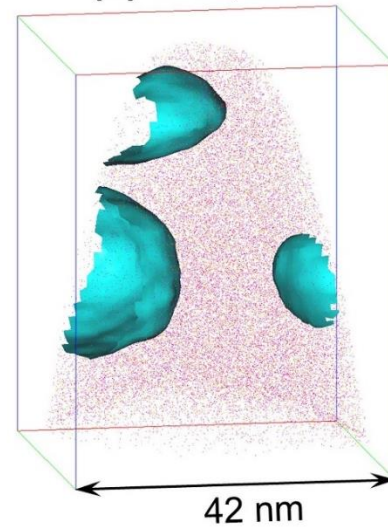
(a) 0Nb, 7.5 min



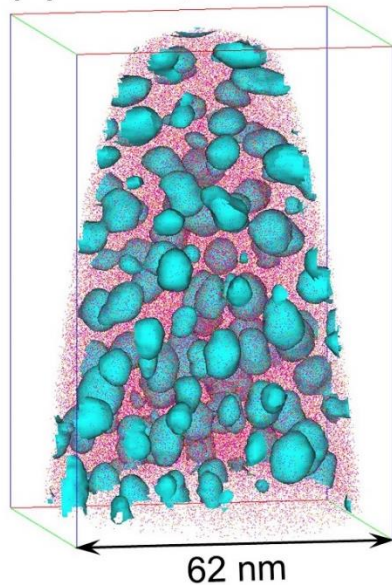
(b) 0Nb, 2 h



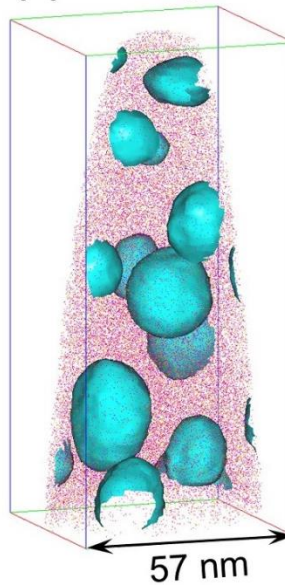
(c) 0Nb, 8 h



(d) 0.8Nb, 7.5 min



(e) 0.8Nb, 2 h



(f) 0.8Nb, 8 h

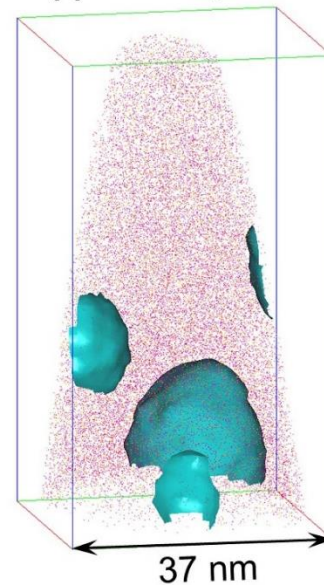


Fig. 6

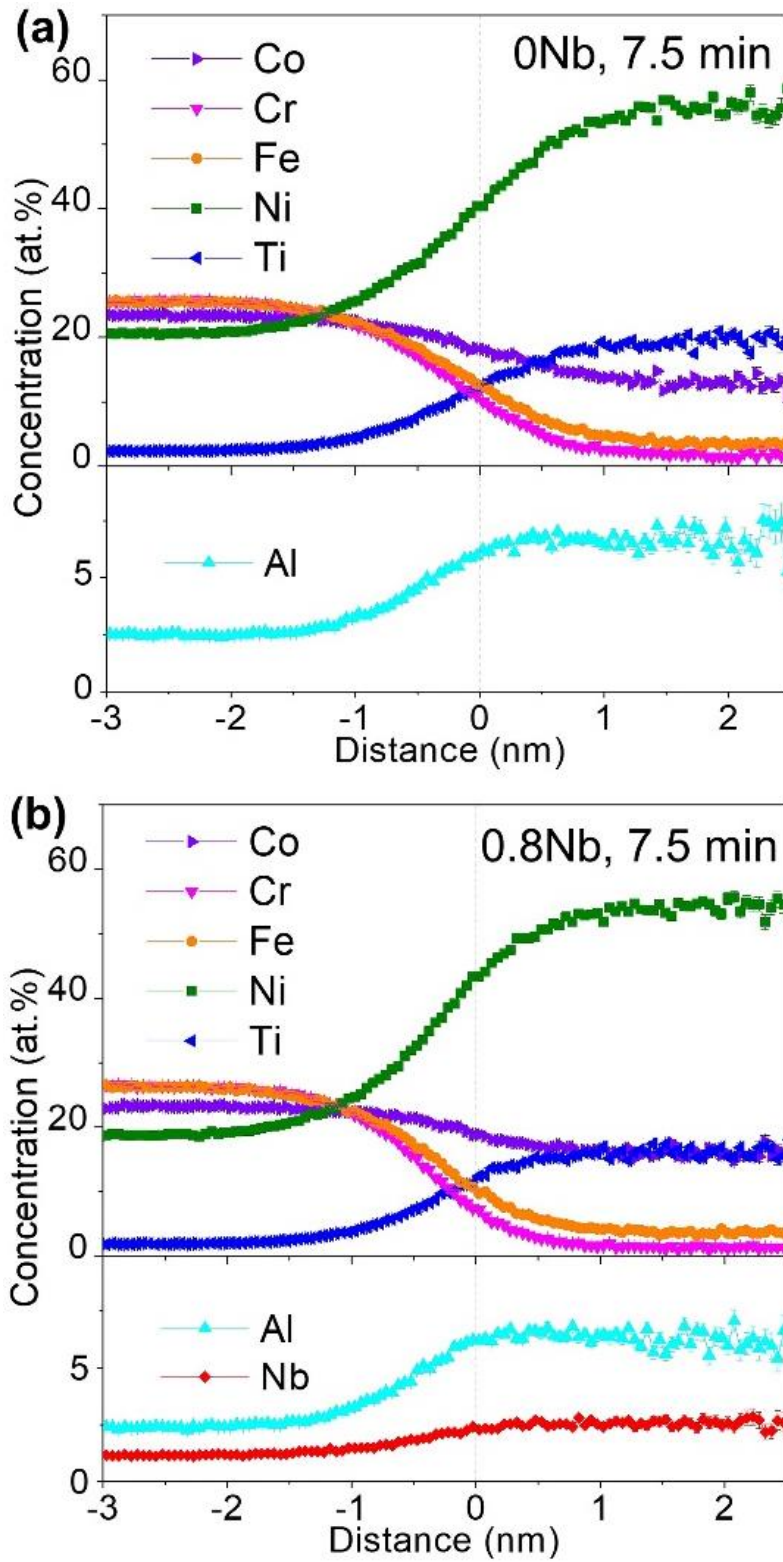


Fig. 6 (cont'd)

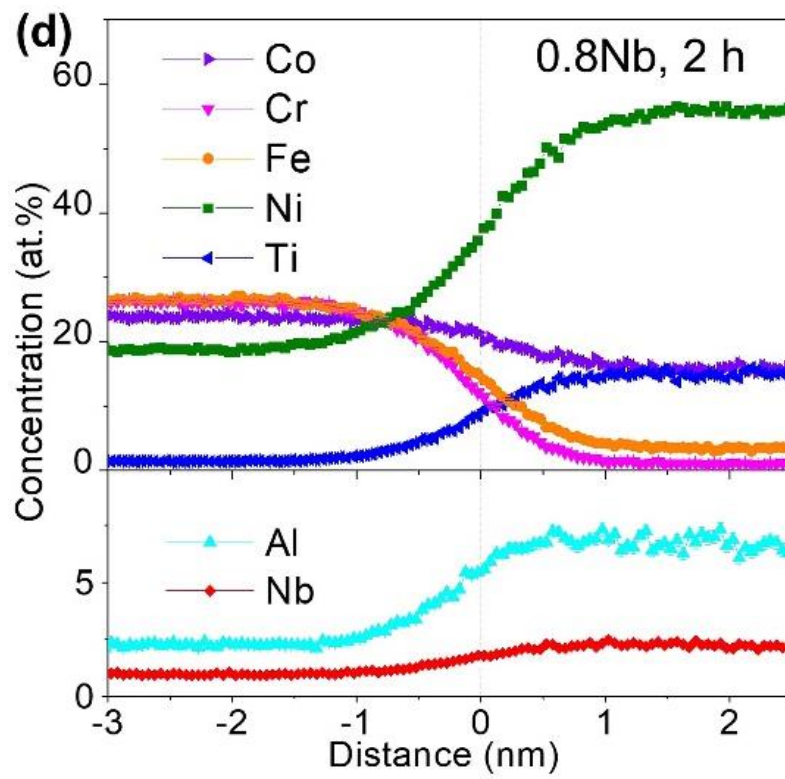
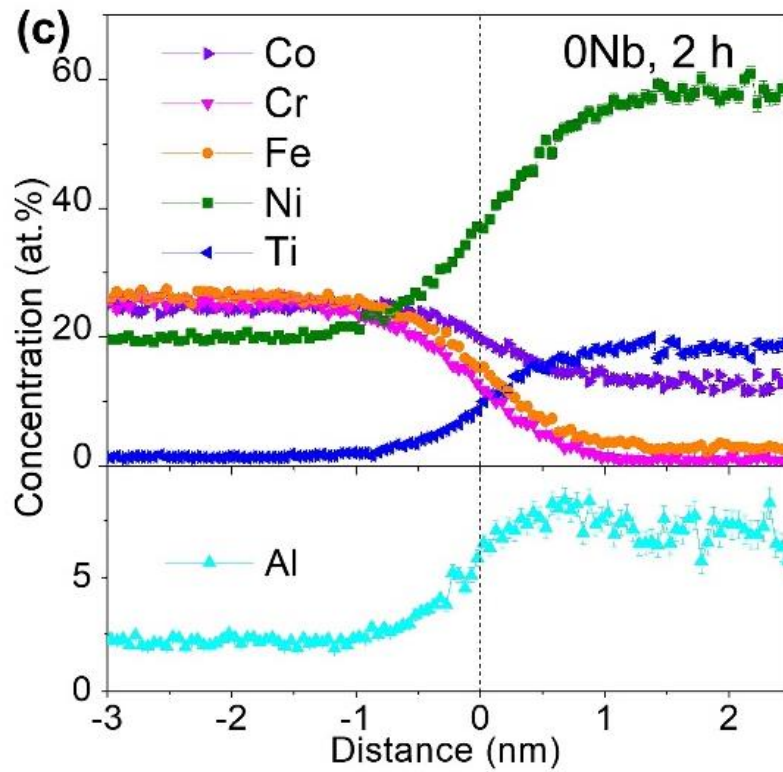


Fig. 6 (cont'd)

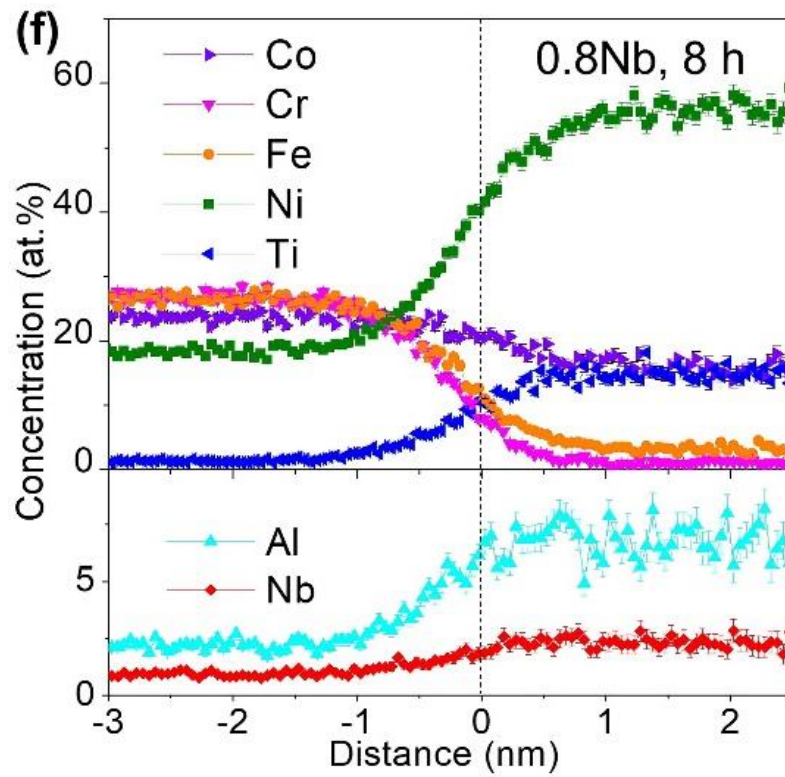
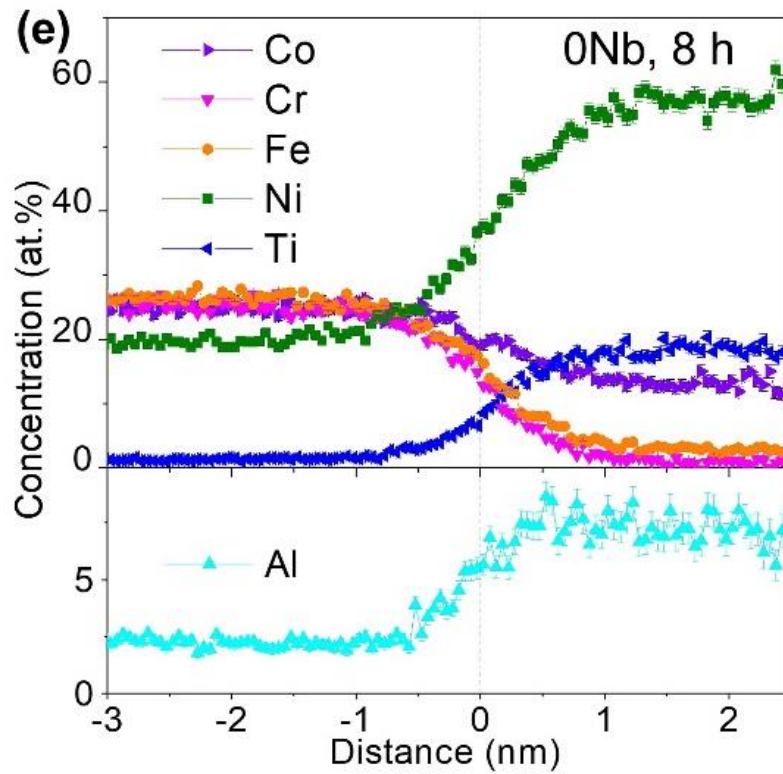


Fig. 7

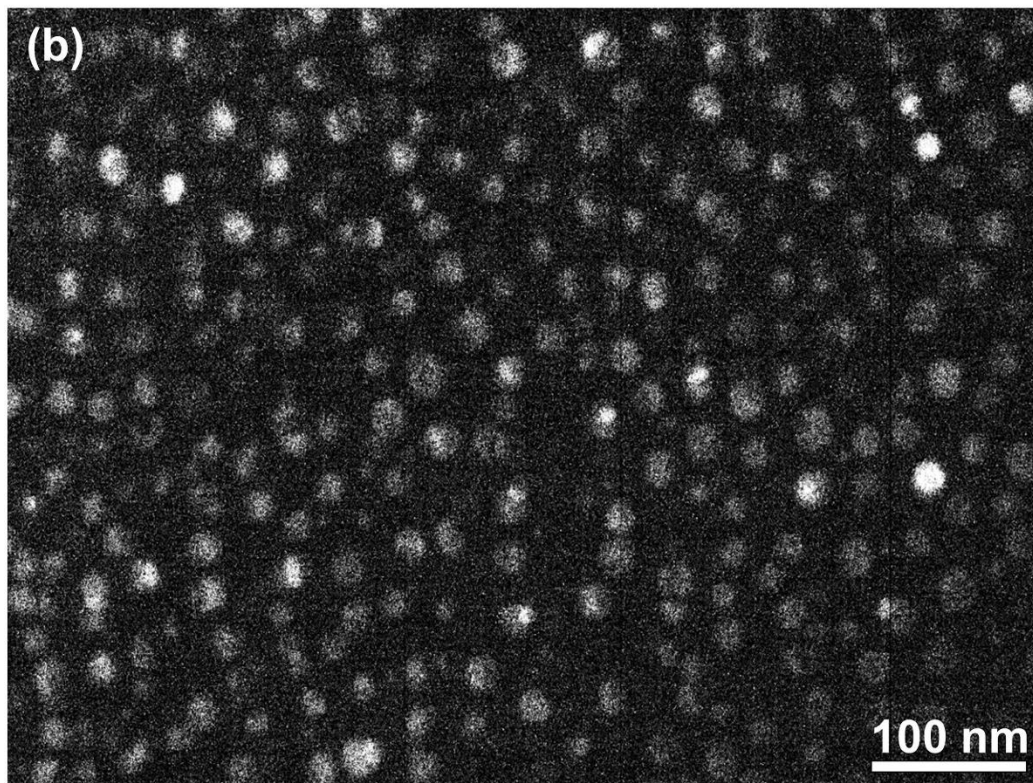
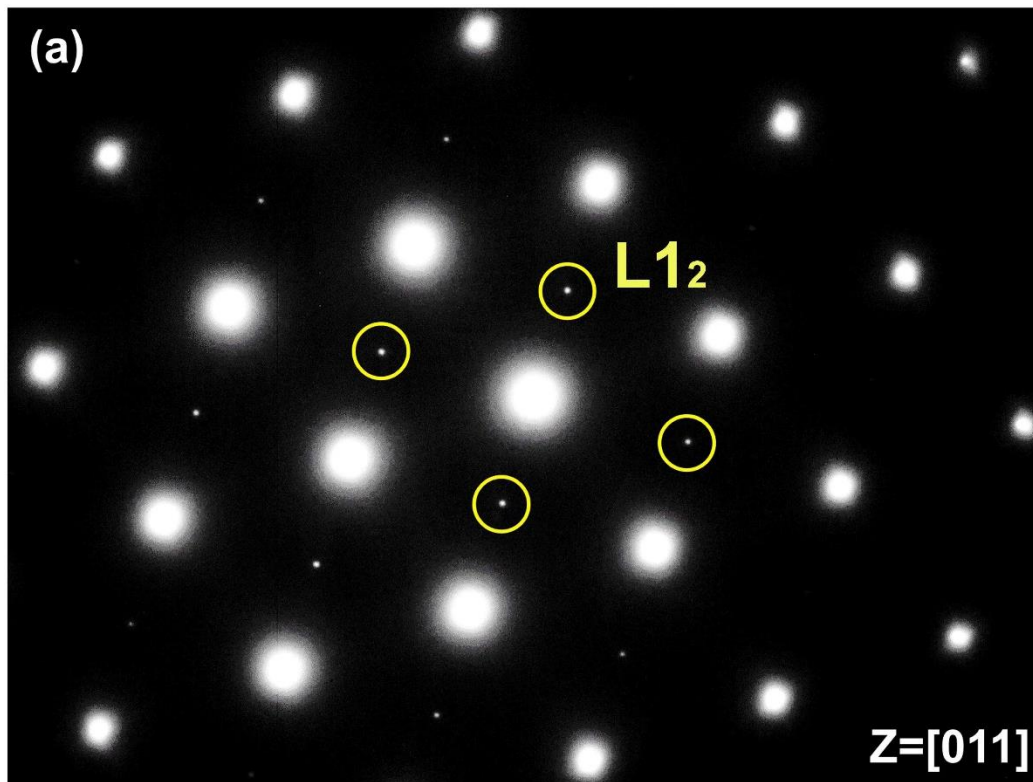


Fig. 8

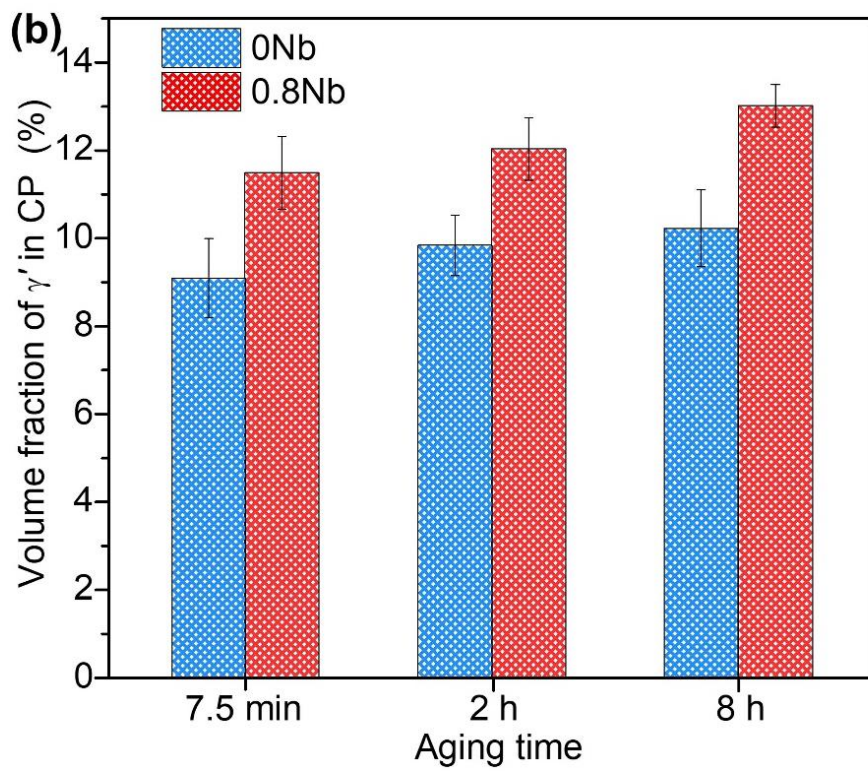
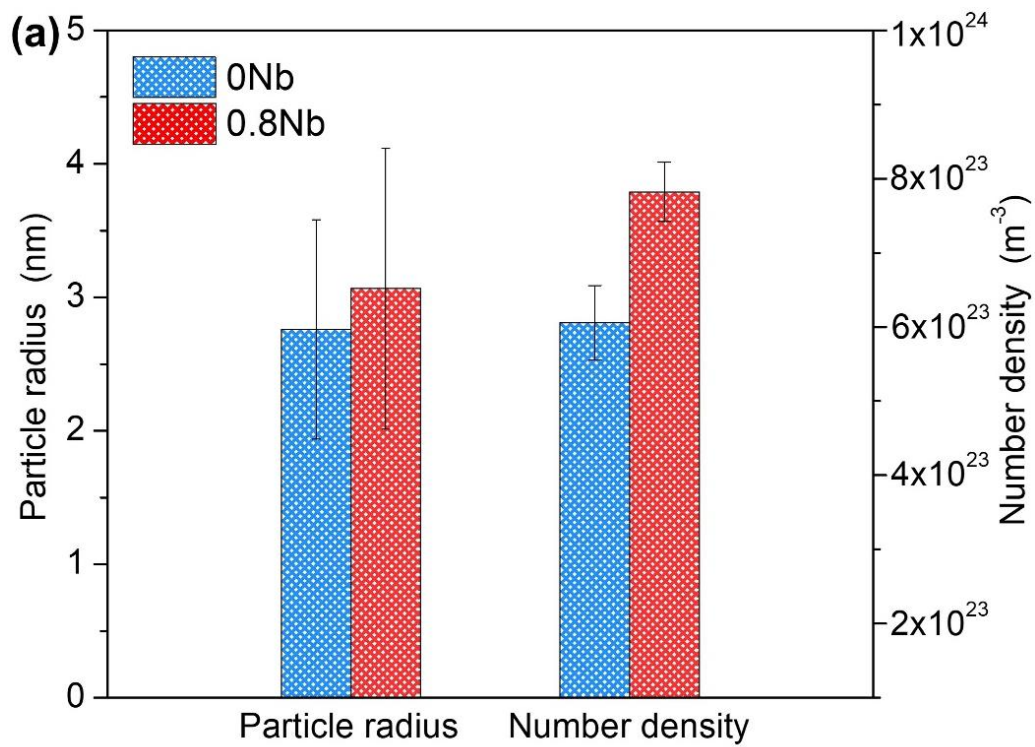


Fig. 9

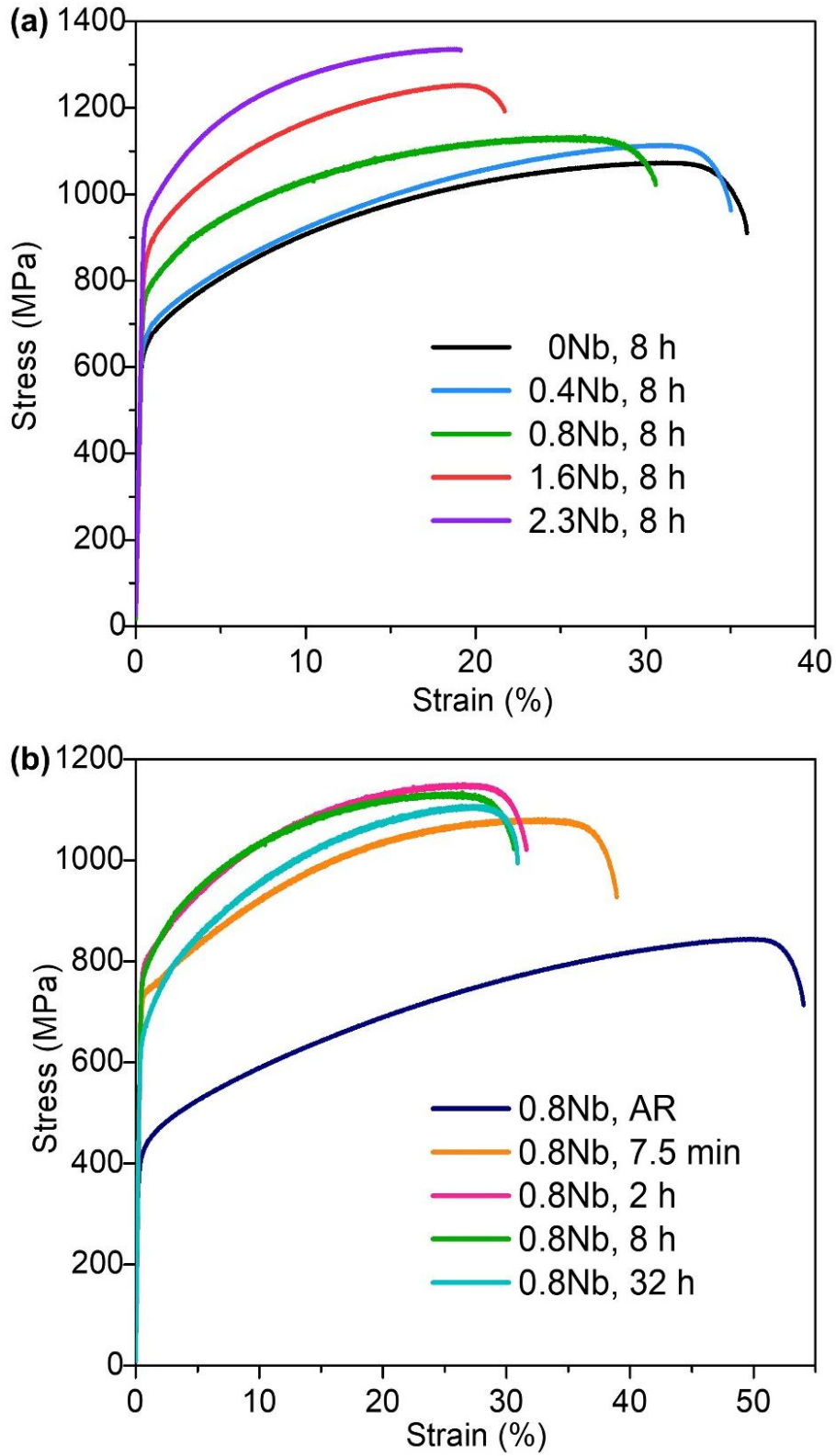


Fig. 10

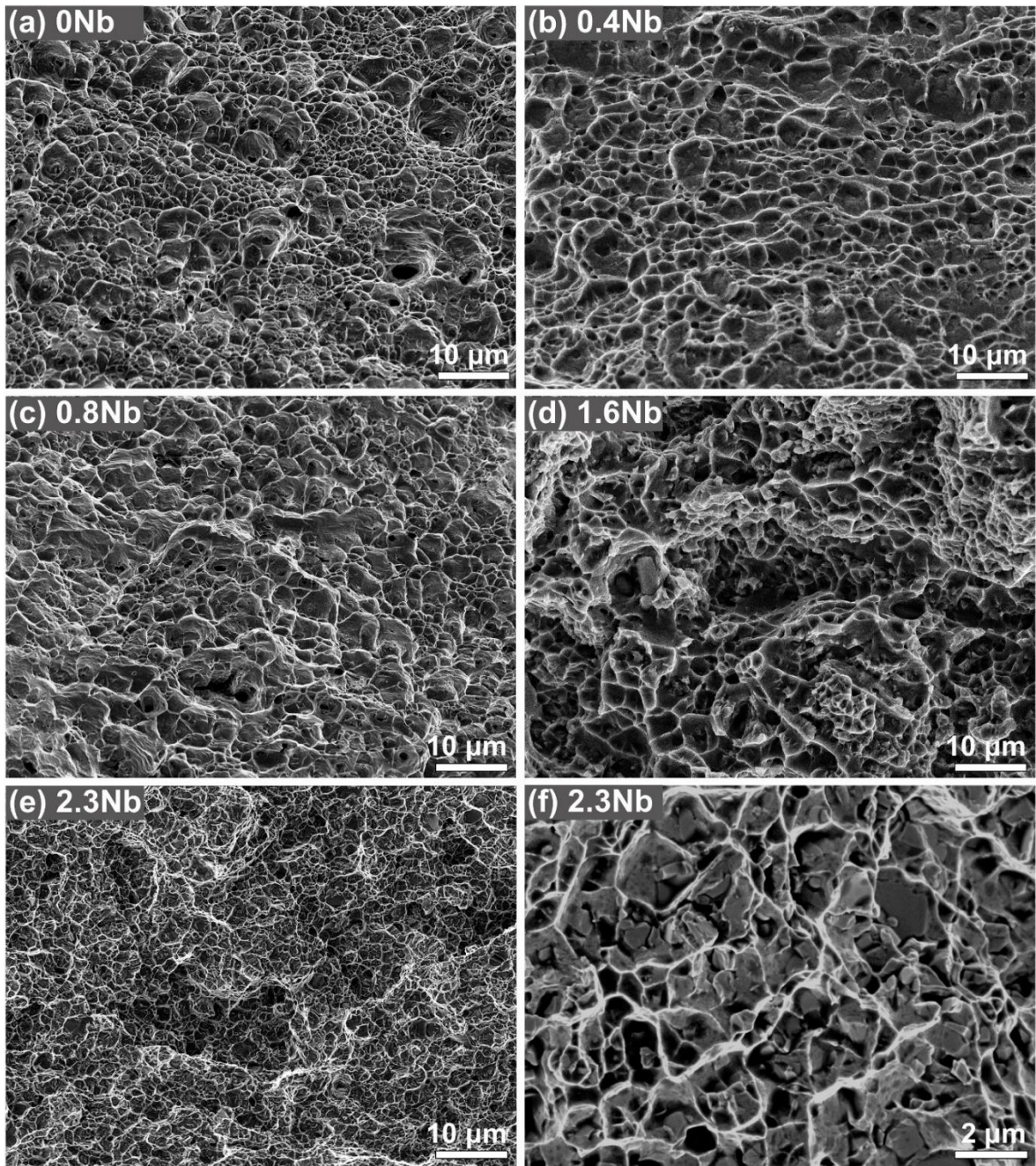


Fig. 11

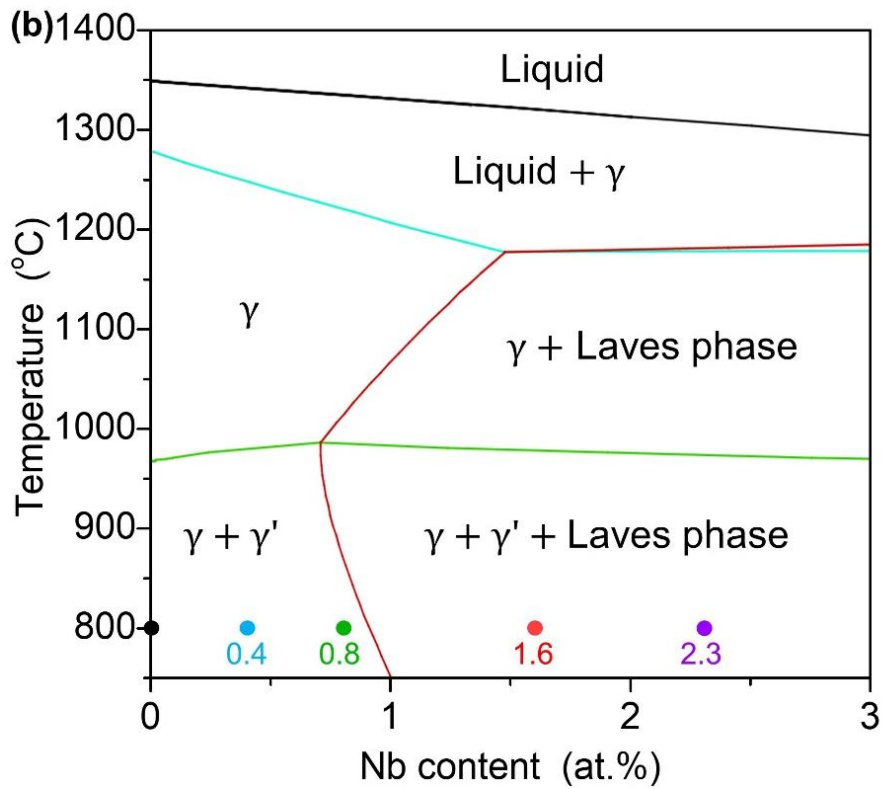
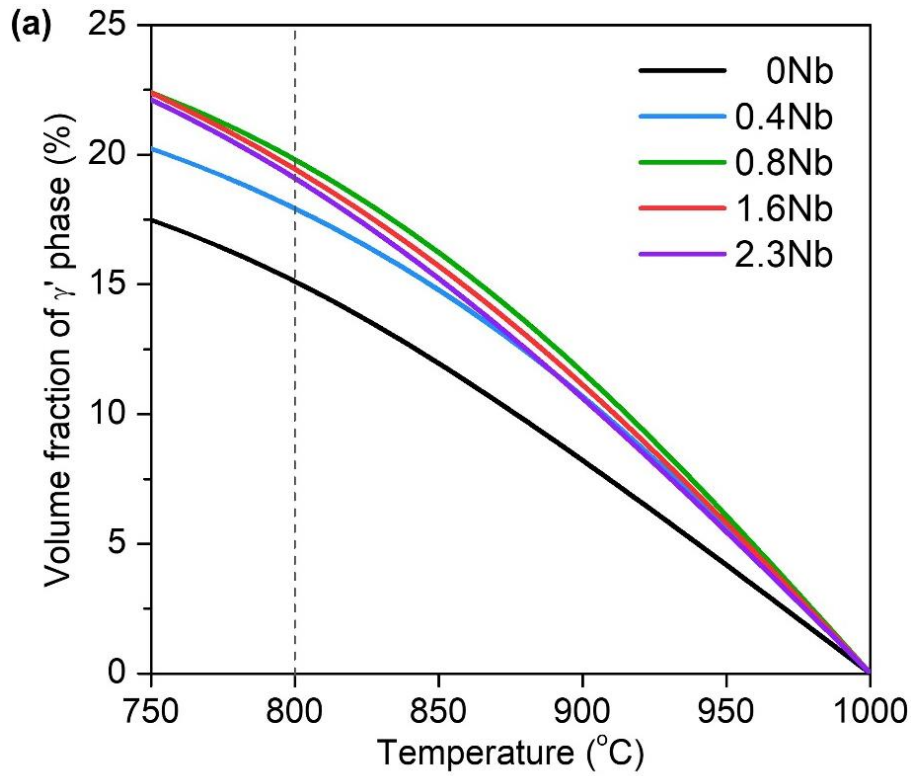
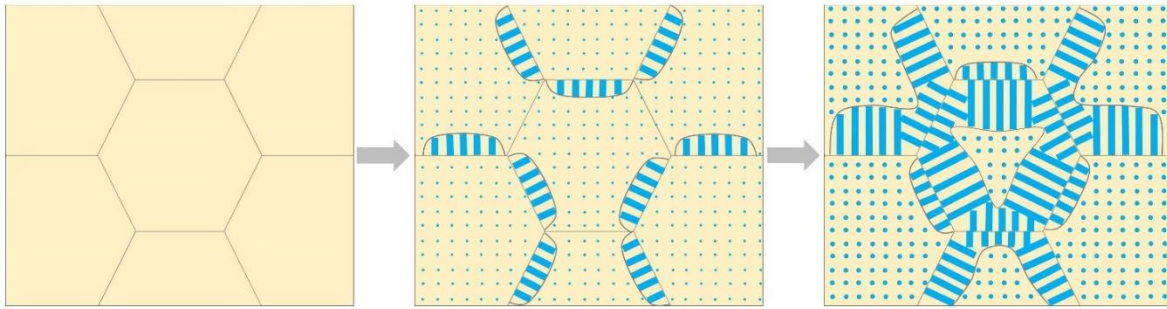
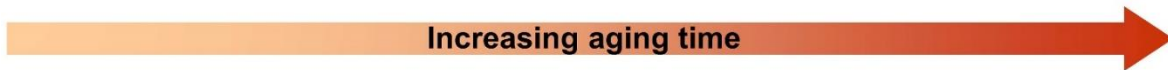
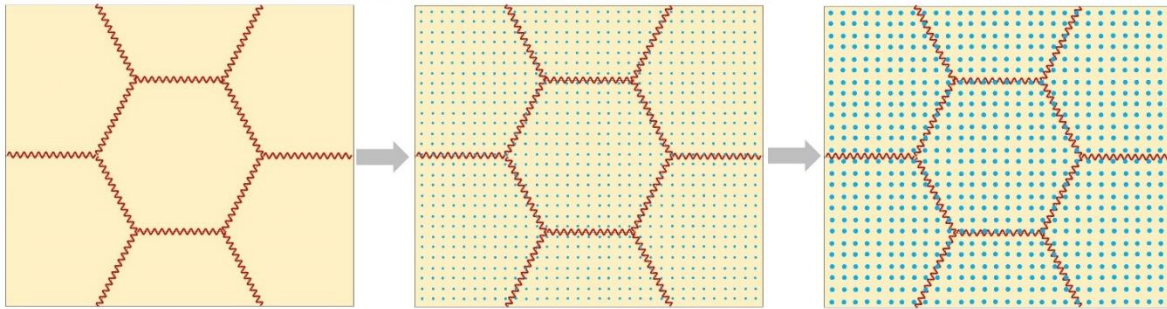




Fig. 12

Nb-free HEAs strengthened by continuous and discontinuous γ' precipitates



Nb-modified HEAs strengthened by continuous γ' precipitates



-  Continuous γ' precipitate
-  Discontinuous γ' precipitate

 Nb segregation at grain boundaries